Available online at www.sciencedirect.com

ScienceDirect

Geochimica et Cosmochimica Acta 253 (2019) 39–62

Geochimica et Cosmochimica Acta

www.elsevier.com/locate/gca

A novel framework for interpreting pyrite-based Fe isotope records of the past

Muammar Mansor *, Matthew S. Fantle *

Department of Geosciences, Pennsylvania State University, University Park, PA 16802, United States

Received 12 November 2018; accepted in revised form 11 March 2019; Available online 19 March 2019

Abstract

The variation in the iron isotopic composition ($\delta^{56}Fe$) of sedimentary pyrite is often interpreted to reflect the degree of Fe redox cycling in modern and ancient environments. However, the degree to which precipitation pathways, isotopic exchange, and precipitation rates can affect the isotopic fractionation associated with pyrite precipitation from aqueous Fe(II) ($Fe(II)_{aq}$) is poorly understood. In this study, pyrite is precipitated at 80 °C in batch reactors through the H_2S and polysulfide pathways, in which the precipitation rates and the concurrent formation of a greigite (Fe_3S_4) phase is modulated by the amount of initially added elemental sulfur and aqueous molybdenum. Our results indicate an average apparent isotopic fractionation ($\delta^{56}Fe_{pyrite}$ - $\delta^{56}Fe_{FeSx}$, where FeS_x includes FeS, $Fe(II)_{aq}$, and greigite) of $-0.51 \pm 0.22‰$ throughout the experiments irrespective of precipitation pathways and greigite formation. Early-stage precipitation is associated with ~0.3‰ larger isotopic fractionation than late-stage precipitation, possibly indicating either a rate-dependent kinetic isotope effect (KIE) or a different isotopic fractionation factor for early-stage pyrite nucleation compared to later-stage growth. Overall, the magnitude of the apparent isotopic fractionation is significantly smaller than the <−2‰ isotopic fractionation determined in previous experiments (Guilbaud et al., 2011b). Numerical models indicate that isotopic exchange between pyrite and $Fe(II)_{aq}$ is necessary to explain the experimental data. The inferred rate of isotopic exchange decreases with time in our experiments, likely as a function of particle size, but shows no clear correlation with temperature across different studies. In the presence of isotopic exchange, modeling results indicate that pyrite precipitated from $Fe(II)_{aq}$ may theoretically have $\delta^{56}Fe$ values ranging from −3 to + 4‰, which spans nearly the whole $\delta^{56}Fe$ range observed in nature. Negative values reflect the expression of the KIE when isotopic exchange is slow (relative to net precipitation rate) while positive values reflect the expression of the equilibrium isotope effect (EIE) when isotopic exchange is relatively fast. We therefore propose that the variation in sedimentary pyrite $\delta^{56}Fe$ can be explained in terms of varying expression of the KIE and the EIE, either during different stages of precipitation or as controlled by the availability of Fe(II), sulfide, and oxidants throughout Earth's history. The predominantly negative (but highly variable) pyrite $\delta^{56}Fe$ values in modern marine sediments suggest a higher expression of the KIE in low temperature systems, but do not rule out the importance of isotopic exchange. The isotopic exchange rate is currently underconstrained in low temperature systems with an uncertainty range that spans 8 orders of magnitude. Our work suggests that isotopic exchange has the potential to affect sedimentary pyrite $\delta^{56}Fe$ unless the current upper limit for isotopic exchange rate is overestimated by 5 orders of magnitude.
© 2019 Elsevier Ltd. All rights reserved.

keywords: Fe isotopes; pyrite; greigite; numerical modeling; kinetic isotope effect; equilibrium isotope effect

* Corresponding authors at: Department of Geological Sciences, University of Texas at El Paso, El Paso, TX 79968, United States (M. Mansor).

E-mail addresses: mbmansor@utep.edu (M. Mansor), msf17@psu.edu (M.S. Fantle).

https://doi.org/10.1016/j.gca.2019.03.017
0016-7037/© 2019 Elsevier Ltd. All rights reserved.

1. INTRODUCTION

Over the past twenty years, advances in mass spectrometric techniques have opened the exciting possibilities of using Fe isotopes (δ^{56}Fe) to trace Fe cycling in a range of natural systems. Significant Fe isotopic fractionation is induced by redox changes between aqueous Fe(II) and Fe(III) and adsorption of Fe(II) onto Fe(III)-oxides, resulting in $Fe(II)_{aq}$ with δ^{56}Fe values that are 1–3‰ lower than Fe(III)-species at equilibrium (Johnson et al., 2002; Welch et al., 2003; Croal et al., 2004; Icopini et al., 2004; Teutsch et al., 2005; Balci et al., 2006; Crosby et al., 2007; Domagal-Goldman and Kubicki, 2008; Wu et al., 2009; Beard et al., 2010; Kappler et al., 2010; Tangalos et al., 2010; Percak-Dennett et al., 2011). Comparatively, other non-redox processes such as diffusion (Rodushkin et al., 2004), aqueous speciation (Dideriksen et al., 2008; Domagal-Goldman and Kubicki, 2008; Fujii et al., 2014), biological uptakes, (Guelke and Von Blanckenburg, 2007; Wasylenki et al., 2007; Kiczka et al., 2010; Mulholland et al., 2015) and various mineral precipitation and dissolution reactions (Brantley et al., 2001, 2004; Skulan et al., 2002; Fantle and DePaolo, 2004; Wiesli et al., 2004; Butler et al., 2005; Johnson et al., 2005; Wiederhold et al., 2006; Guilbaud et al., 2011a; Liermann et al., 2011; Wu et al., 2012; Yesavage et al., 2012; Shi et al., 2016; Wolfe et al., 2016) generate small ($\leq$1‰) fractionations. Thus, Fe isotopic fractionations larger than 1‰ observed in nature have been proposed to reflect redox changes driven by either environmental variables (e.g., oxygen variation at global or local spatial scales) or microbial iron reduction (e.g., Yamaguchi et al., 2005; Johnson et al., 2008; Severmann et al., 2008; Teutsch et al., 2009; Czaja et al., 2010, 2012; Ohmoto et al., 2014; Kunzmann et al., 2017).

Among Fe-bearing minerals, pyrite (FeS_2) displays the largest natural δ^{56}Fe variation ranging from −4 to +4‰, which has been interpreted in terms of redox cycling of Fe coupled with pyrite precipitation from either negative δ^{56}Fe $Fe(II)_{aq}$ or positive δ^{56}Fe Fe(III) sources (Graham et al., 2004; Rouxel et al., 2004, 2005, 2008; Archer and Vance, 2006; Severmann et al., 2006, 2008; Fehr et al., 2010; Nishizawa et al., 2010; Yoshiya et al., 2012; Percak-Dennett et al., 2013; Virtasalo et al., 2013; Busigny et al., 2014; Dziony et al., 2014; Marin-Carbonne et al., 2014; Scholz et al., 2014; Agangi et al., 2015; Lin et al., 2017; Toner et al., 2016; Wolfe et al., 2016; Galić et al., 2017; Sawaki et al., 2018). However, the interpretation of pyrite δ^{56}Fe is not straightforward as pyrite can precipitate through multiple pathways, with potentially distinct isotopic fractionations associated with each pathway. Under sulfide-rich conditions, the precipitation of pyrite starts from the speciation of $Fe(II)_{aq}$ (defined as total aqueous Fe(II)) to aqueous FeS (FeS_{aq}) clusters (Rickard et al., 2001):

$$Fe^{2+} + H_2S \rightarrow FeS_{aq} + 2H^+ \quad (1)$$

In laboratory experiments, the mineral FeS (mackinawite) is typically used as an Fe(II) source, which, upon dissolving, releases FeS_{aq} that reacts with reduced sulfur to form pyrite either through the H_2S pathway (Rickard, 1997):

$$FeS_{aq} + H_2S \rightarrow FeS_2 + H_2 \quad (2)$$

or the polysulfide pathway (Rickard, 1975; Luther, 1991):

$$H_2S + S(0) \rightarrow S_2^{2-} + 2H^+ \quad (3)$$

$$FeS_{aq} + S_2^{2-} \rightarrow FeS_2 + S^{2-} \quad (4)$$

Occasionally, pyrite formation under these conditions proceeds through a greigite (Fe_3S_4) intermediate phase (Schoonen and Barnes, 1991; Wang and Morse, 1996; Wilkin and Barnes, 1996; Morse and Wang, 1997). The third pathway for pyrite precipitation has been recently termed as the ferric-hydroxide-surface (FHS) pathway (Peiffer et al., 2015; Wan et al., 2017), although tentative evidence for this pathway has been described even earlier (Canfield, 1989). The FHS pathway dominates when Fe(III) (aqueous and solid phases) concentrations exceed those of sulfide, primarily in oxic-to-suboxic environments such as marshes, lake sediments, and the top few centimeters of marine sediments. In regions containing high concentration of sulfides such as euxinic water bodies or in the sulfate reduction zones of sedimentary columns, pyrite precipitation will likely proceed predominantly through the H_2S and polysulfide pathways (Peiffer et al., 2015; Wan et al., 2017).

To date, only a few studies have attempted to constrain the isotopic fractionation associated with pyrite precipitation. Guilbaud et al. (2011b) measured apparent isotopic fractionations of -2.65 ± 0.34‰ and -2.07 ± 0.22‰ (relative to the initial FeS mineral and $Fe(II)_{aq}$) at 40 °C and 100 °C, respectively, for the H_2S precipitation pathway. Rolison et al. (2018) inferred an apparent fractionation of -2.75 ± 0.22‰ for pyrite precipitation from $Fe(II)_{aq}$ in the Black Sea, by assuming that the progressive increase in the δ^{56}Fe of $Fe(II)_{aq}$ in the euxinic water column was caused primarily by pyrite precipitation. This isotopic fractionation likely reflects the combined expression of the H_2S and polysulfide pathways. At higher temperatures (300–350 °C), Syverson et al. (2013) measured an apparent fractionation of −1.1 to −0.2‰ during early stages (<1 h) of pyrite precipitation from $Fe(II)_{aq}$. The apparent fractionation increased with time up to +1‰ due to continuous isotopic exchange between pyrite and residual $Fe(II)_{aq}$ over a period of ~1000 h, consistent with the predicted direction of equilibrium isotopic fractionation between $Fe(II)_{aq}$ and pyrite (Blanchard et al., 2009; Rustad et al., 2010; Polyakov and Soultanov, 2011).

Considering all the available data, a trend emerges whereby the Fe isotopic fractionation associated with pyrite precipitation correlates with an increase in temperature (Fig. 1). Similar temperature-dependent trends have been observed for calcium and silicon isotopic fractionation during calcite and amorphous silica precipitation, respectively (e.g., Tang et al., 2008; Roerdink et al., 2015). These trends have been explained in terms of the surface kinetic model (Fantle and DePaolo, 2007; DePaolo, 2011), which posits that the isotopic composition of a mineral is a function of the kinetic isotope effect (KIE) imparted during rapid precipitation and a concurrent equilibrium isotope effect (EIE) associated with mineral-fluid isotopic exchange. As temperature increases, the isotopic exchange rate increases

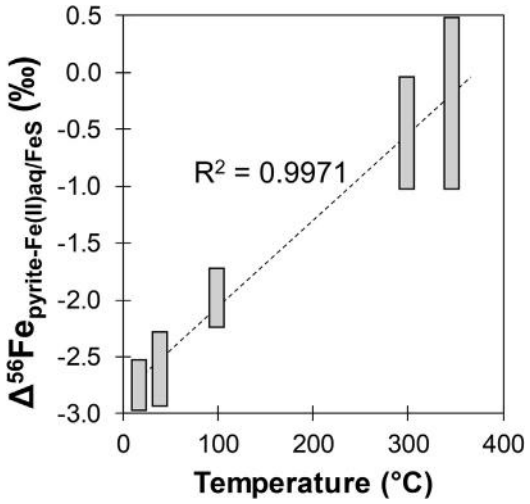

Fig. 1. The apparent relationship between temperature and Fe isotopic fractionation associated with pyrite precipitation. Data at various temperatures from Guilbaud et al. (2011b), Syverson et al. (2013) and Rolison et al. (2018).

such that the isotopic fractionation approaches the maximum EIE, which explains the observed relationship between the apparent isotopic fractionation and temperature. It is known that pyrite can isotopically exchange with $Fe(II)_{aq}$ at temperatures $\geq$300 °C (Syverson et al., 2013; Dziony et al., 2014), but there remains a real question as to whether this process can occur at a significant rate at lower temperatures applicable to experiments and sedimentary settings. If isotopic exchange can impact the apparent isotopic fractionation associated with sedimentary pyrite precipitation or alters the isotopic composition post-precipitation, this effect must be quantified in order to interpret Fe isotope records with confidence.

In this study, we seek to understand the potential effects of precipitation pathways and isotopic exchange on the Fe isotopic fractionation associated with pyrite precipitation. To this end, we precipitated pyrite via the H_2S pathway in batch reactors under conditions comparable to Guilbaud et al. (2011b), except at precipitation rates that were approximately three orders of magnitude slower. We hypothesize that the effects of isotopic exchange are more pronounced during slow precipitation and can be evaluated more easily under such conditions. We also precipitated pyrite through the polysulfide pathway, in which the precipitation rates and the formation of a greigite phase is modulated by the amount of added elemental sulfur (S(0)) and aqueous molybdenum. Our results suggest an average apparent isotopic fractionation of -0.51 ± 0.22‰ for pyrite precipitation irrespective of precipitation pathways and greigite formation. The measured apparent isotopic fractionation is substantially smaller than previous experiments (Guilbaud et al., 2011b). Modeling results indicate that isotopic exchange between pyrite and $Fe(II)_{aq}$ is necessary to explain the experimental data, and that this process occurs at temperatures as low as 80 °C in experimental systems. Extrapolating to lower temperatures, we propose that the balance between the expression of the KIE and the EIE under different environmental conditions can account for nearly the whole δ^{56}Fe range of sedimentary pyrite without the need to invoke any positive δ^{56}Fe Fe(III) sources for pyrite precipitation.

2. MATERIALS AND METHODS

2.1. Experimental pyrite precipitation, sampling, and chemical analyses

All steps were performed in an anaerobic chamber (98% N_2 – 2% H_2 atmosphere) unless otherwise specified. Solutions were prepared fresh for all experiments and rendered anoxic by degassing with N_2 for at least 20 minutes. Four stock solutions were prepared: (i) 3 mM Fe(II) [$(NH_4)_2Fe(SO_4)_2{\cdot}6H_2O$; J.T. Baker Chemicals, product # 2054] dissolved in 20 mM NaCl, (ii) 1 M MOPS buffer adjusted to pH 7 with NaOH, (iii) 180 mM $Na_2S.9H_2O$ (EMD Chemical, product # SX0770), and (iv) either 3 or 3,000 µM sodium molybdate ($Na_2MoO_4.2H_2O$; Alfa Aesar, CAS# 10102-40-6).

Five different experiments (denoted 'H_2S', 'PS10', 'PS500', 'PSG0.1', and 'PSG100') were conducted. First, pyrite was precipitated through the H_2S pathway ('H_2S' experiment) by adding 1.5 ml of MOPS and 1 ml of $Na_2S{\cdot}9H_2O$ to 30 ml of Fe(II) stock solution. The final concentration of Fe and sulfide was ~3 mM and ~6 mM, respectively. The batch reactor (50 ml volume acid-cleaned glass vials) was immediately sealed with Butyl-septa and aluminum caps. Next, pyrite precipitation via the polysulfide pathway was induced by adding S(0) at either 10 or 500 mM ('PS10' and 'PS500' experiments) to the starting Fe(II)-sulfide-MOPS mixture. Finally, pyrite precipitation with greigite formation was achieved by adding either 0.1 or 100 µM molybdenum in the presence of 10 mM S(0) ('PSG0.1' and 'PSG100' experiments). Pyrite precipitation was allowed to proceed without stirring at 80 °C for up to one week. In the 'PS' and 'PSG' experiments, the solutions developed a yellowish coloration after a few hours of incubation at 80 °C, indicating the presence of polysulfides (Fig. EA-1; Kamyshny et al., 2004).

Reaction progress (i.e., pyritization extent) was tracked through sacrificial sampling of parallel batch reactors at different time points. Prior to sampling, a hand magnet was used to test for the presence of magnetic greigite. Reactors were then uncapped and the contents transferred to 50 ml tubes for separation of FeS_x species ($Fe(II)_{aq}$, FeS, and greigite) and pyrite based on a modified sequential acid extraction method (Huerta-Diaz and Morse, 1990; Guilbaud et al., 2011b). First, ~6 ml of concentrated HCl was added to achieve a final concentration of 2 N HCl. Both FeS and greigite (when present) were dissolved for 2 hours while being continuously shaken. Samples were then centrifuged at 8,000g for 15 min and the supernatants transferred to a storage tube. Residuals were washed twice more, with 10 ml 2 N HCl and 10 ml H_2O, centrifuged in between, and the supernatants combined with the first HCl extract. No magnetism was detected in the solid residuals after HCl extraction, indicating that greigite fully dissolved in HCl. The remaining solid residuals were then treated with

5 ml 15 N HNO_3 to dissolve pyrite. Iron concentrations were measured in each extract with the Hach FerroVer method (Hach Co., Loveland, CO, USA); these data were subsequently used to calculate the pyritization extent:

$$\text{Pyritization extent} = Fe_{pyrite}/(Fe_{pyrite} + Fe_{FeSx}) \quad (5)$$

Initial tests of the sequential acid extraction on powdered pyrite (nodule from Spain, mineralogy confirmed by X-ray diffraction) indicated that at most 0.25% of the pyrite-Fe was released into solution during the HCl step. Instantaneous pyrite precipitation rates ($R_{ppt\text{-}inst}$) were calculated between adjacent time points assuming a linear trend within that time period. Estimated errors for pyritization extent and precipitation rates were ≤ 0.03 and $\leq 0.06 \cdot 10^{-8}$ mol/L/s, respectively, based on replicate runs.

X-ray diffraction (XRD) analyses were used to identify the mineral products from parallel incubations. Solid samples were pelletized at 8000g for 15 min in rubber-lined sealed tubes and the supernatants decanted in an anaerobic chamber. Not all solid materials pelletize during this step; solids at low pyritization extent were particularly resistant to settling, most likely because they were comprised of nanoparticulate FeS. Thus, our XRD data cannot be considered to be quantitative. Visible pellets were nonetheless obtained in all cases. These pellets were frozen at −20 °C and freeze-dried under vacuum. Diffraction patterns of dried samples were collected from 0 to 70° 2θ using a PANalytical Empyrean X-ray diffractometer. The total collection time was 30 min, which was well below the time frame (~7 days) over which dried mackinawite starts to oxidize in air to form elemental sulfur, greigite, and/or Fe-oxides (Boursiquot et al., 2001). Mineral phases were finally identified using the database in the Jade software package (MDI Products).

2.2. Iron isotopic analysis and notation

About 15–30 µg of Fe (from the HCl or HNO_3 extracts) was dried down at 80 °C in Teflon vials and treated twice with 250 µl of 30% hydrogen peroxide and 250 µl of concentrated HNO_3 in order to fully oxidize Fe(II) to Fe (III). After dry down, samples were resuspended in 7 N HCl and Fe was purified by ion exchange chromatography using AG-MP1 resin to remove matrix elements following established protocol (Yesavage et al., 2016). Column yields were >95% as assessed by quadrupole ICP-MS, thereby ensuring no isotopic fractionation on the column.

Iron isotopic compositions were measured on a Thermo-Fisher Scientific Neptune Plus MC-ICP-MS in the Metal Isotope Laboratory (MIL) at Penn State University. Purified samples were diluted to 3 ppm Fe in a 0.3 N HNO_3 matrix and aspirated using a 100 µl/min PFA nebulizer attached to a quartz dual cyclonic spray chamber for introduction to the instrument. Analyses were conducted in wet plasma mode and high-resolution at 1200 W power. Ion beams corresponding to ^{52}Cr, ^{53}Cr, ^{54}Fe, ^{56}Fe, ^{57}Fe, ^{58}Fe, and ^{60}Ni were monitored on the L4, L2, L1, C, H1, H2, and H4 Faraday cups, respectively, within one measurement block per sample consisting of 35 cycles with a 4.2 s integration time. Typical ion beam voltages for ^{56}Fe under this condition were 12 to 24 V. The reference material IRMM-14 was used as a bracketing standard, and all samples were corrected for mass bias using standard-sample bracketing. The contribution of ^{54}Cr to the ^{54}Fe signal was estimated from the ^{52}Cr and ^{53}Cr intensities assuming either natural or mass bias-corrected abundance ratios. In either case, the $^{54}Cr/^{54}Fe$ ratios for all samples were <0.025 ‰ such that Cr interference corrections changed the $\delta^{56}Fe$ values by <0.03‰. Isotopic compositions are reported in delta (δ) notation in per mil (‰) units:

$$\delta^{56}Fe = [(^{56}Fe/^{54}Fe)_{sample}/(^{56}Fe/^{54}Fe)_{standard} - 1] \cdot 10^3 \quad (6)$$

In-house standards (HPS-Fe – courtesy of Clark Johnson at the University of Wisconsin - and NIST SRM 3126a) were measured in every analytical session, and each sample was measured at least in duplicate. The $\delta^{56}Fe$ values for HPS-Fe and SRM 3126a measured over multiple analytical sessions were 0.55 ± 0.03‰ and 0.33 ± 0.03‰, respectively (2SD external reproducibility; $n = 14$ for each standard), which agreed with the long-term values of 0.60 $\pm$ 0.07‰ for HPS-Fe and 0.34 ± 0.10‰ for SRM 3126a measured in MIL (Yesavage et al., 2016). These values are on the high and low end, respectively, compared to $\delta^{56}Fe$ values measured from other laboratories, with average of 0.48 ± 0.09‰ for HPS-Fe (Beard et al., 2003; Severmann et al., 2006; Czaja et al., 2012; d'Abzac et al., 2014; Liu et al., 2015) and 0.41 ± 0.08‰ for SRM 3126a (Rouxel and Auro, 2010; Chever et al., 2015).

Throughout this paper, the intrinsic isotopic fractionation factor due to a specific kinetic- or equilibrium-controlled process is denoted by the symbol alpha (α), where the subscripts 'a' and 'b' represent two coexisting phases:

$$\alpha_{a-b} = \frac{1000 + \delta^{56}Fe_a}{1000 + \delta^{56}Fe_b} \quad (7)$$

The apparent isotopic fractionation (or isotopic effect) between two phases observed in experimental or natural systems can be a function of multiple processes, each of which has a distinct intrinsic isotopic fractionation factor. In this study, therefore, we use the capital delta (Δ) notation to refer to the observed difference in isotopic composition between two phases:

$$\Delta^{56}Fe_{a-b} = \delta^{56}Fe_a - \delta^{56}Fe_b \quad (8)$$

3. RESULTS

3.1. Precipitation rates, pyritization extent, and greigite formation

Upon addition of sulfide, black precipitates rapidly form in all five of the experiments. This early-formed phase is identified via XRD as poorly crystalline mackinawite (FeS) through a broad peak around 17° 2θ (Lennie, 1995). Over time, pyrite forms at the expense of FeS_x (FeS_x includes FeS, greigite, and $Fe(II)_{aq}$) and the reactions reach pyritization extents of 0.41 to 0.99 after one week depending on the experiments (Table 1). The formation of pyrite is confirmed through XRD (Fig. 2; Fig. EA-2). Pyrite

Table 1
Summary of the sampling time, pyritization extent, precipitation rate ($R_{ppt\text{-}inst}$), and $\delta^{56}Fe$ values for each sample analyzed in this study.

Sample	Time (day)	Pyritization extent	$R_{ppt\text{-}inst}$ [a] (10^{-8} mol/L/s)	$\delta^{56}Fe_{FeSx}$ (‰)	$\delta^{56}Fe_{pyrite}$ (‰)	$\Delta^{56}Fe_{pyrite\text{-}FeSx}$ (‰)	$\delta^{56}Fe_{sum}$ [b] (‰)
Initial Fe salt	–	–	–	–	–	–	0.44
Initial FeS	0	0.00	–	0.45	–	–	0.45
H_2S	0.33	0.04	1.57	0.48	−0.28	−0.76	0.45
H_2S pathway,	1	0.23	0.81	0.58	−0.03	−0.61	0.44
Fe(II) + S(−II)	7	0.41	0.09	0.47	0.22	−0.25	0.37
					Average	**−0.54 ± 0.21**	
PS10	1	0.27	0.94	0.66	−0.37	−1.03	0.39
Polysulfide	3	0.44	0.27	0.64	0.19	−0.45	0.44
pathway,	5	0.71	0.41	0.74	0.33	−0.41	0.45
+ 10 mM S(0)	7	0.83	0.18	0.85	0.35	−0.50	0.44
					Average	**−0.59 ± 0.25**	
PS500	1	0.34	1.19	0.63	0.06	−0.57	0.44
Polysulfide	3	0.62	0.44	0.63	0.38	−0.25	0.48
pathway,	5	0.78	0.24	0.69	0.39	−0.31	0.45
+ 500 mM S(0)	7	0.94	0.24	0.93	0.41	−0.52	0.44
					Average	**−0.41 ± 0.14**	
PSG0.1	1	0.31	1.10	0.69	−0.04	−0.73	0.46
With greigite,	3	0.48	0.25	0.67	0.18	−0.49	0.44
+ 10 mM S(0)	5	0.80	0.49	0.69	0.36	−0.33	0.42
+ 0.1 μM Mo	7	0.95	0.22	0.56	0.46	−0.10	0.46
					Average	**−0.41 ± 0.23**	
PSG100	1	0.37	1.31	0.70	0.03	−0.68	0.45
With greigite,	3	0.57	0.30	0.82	0.21	−0.61	0.47
+ 10 mM S(0)	5	0.89	0.49	0.99	0.39	−0.59	0.46
+ 100 μM Mo	7	0.99	0.15	*1.31*[c]	0.51	*−0.79*[c]	0.52
					Average	***−0.63 ± 0.04***[c]	

[a] 1SD for instantaneous precipitation rate ($R_{ppt\text{-}inst}$) is $<0.06 \cdot 10^{-8}$ mol/L/s based on measurements from duplicate reactors.
[b] $\delta^{56}Fe_{sum}$ values for the initial Fe salt and initial FeS are based on their respective measured $\delta^{56}Fe$, with typical 2SD of ≤0.08‰. $\delta^{56}Fe_{sum}$ values for the rest of the samples were calculated from isotopic mass balance, with propagated 2SD of ≤0.11‰.
[c] The $\delta^{56}Fe$ value of FeS_x may be compromised by trace Fe released during pyrite dissolution in HCl. This datum is therefore omitted for the average $\Delta^{56}Fe_{pyrite\text{-}FeSx}$ calculation.

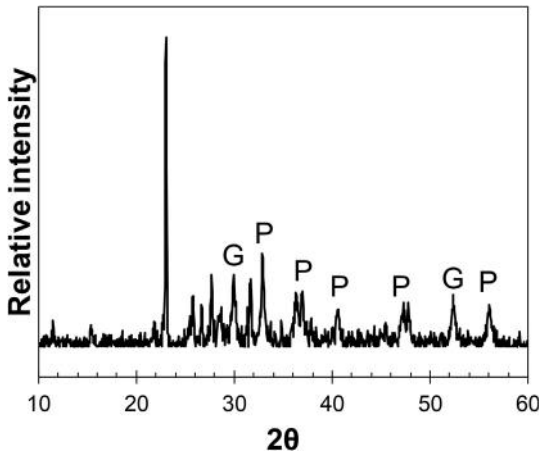

Fig. 2. XRD pattern of the reaction products from 'PSG100' experiment after three days of incubation. Pyrite (P) and greigite (G) are detectable. Unlabeled peaks belong to elemental sulfur and halite formed during drying.

precipitation rates range from 0.09 to $1.57 \cdot 10^{-8}$ mol/L/s, with rates being higher at the beginning and decreasing by about an order of magnitude over the course of precipitation (Table 1; Fig. 3).

In the 'H_2S' experiment, incomplete pyritization is observed with a maximum pyritization extent of 0.41 after one week (Fig. 3a and b). In contrast, precipitation in the presence of S(0) ('PS10' and 'PS500' experiments) leads to an overall increase of pyritization extent with a maximum of 0.94 after one week. Initial rates (at pyritization extents $\leq$0.34) for the 'PS' experiments are faster by 16 to 47% relative to the 'H_2S' experiment, with faster rates correlating with higher initial S(0) (Table 1).

In the presence of S(0), the addition of aqueous molybdenum leads to even higher pyritization extents and precipitation rates, and also induces greigite formation. These effects are not observed in the absence of S(0). Pyritization extents up to 0.99 are achieved and initial precipitation rates (at pyritization extents $\leq$0.37) are faster by 17–39% compared to the 'PS10' experiment. The presence of greigite in these experiments is first noticed through strong magnetism of the solid reaction products after just one day of incubation. The loss of magnetism after treatment with 2 N HCl suggests that it is a property of a HCl-soluble phase such as greigite (Rickard and Morse, 2005). XRD analyses reveal a peak at 2θ of ~30° (and occasionally a smaller peak at ~53° 2θ) that is consistent with the presence of greigite (Fig. 2; Fig. EA-2).

3.2. Iron isotopic compositions

The δ^{56}Fe values of both FeS_x and pyrite are analyzed at several time points within each experiment. The Fe isotopic compositions of all samples fall along the mass dependent fractionation line (Fig. EA-3) and isotopic mass balance is achieved in all extractions (Table 1). At pyritization extents $\leq$0.95, trace Fe released from pyrite dissolution in HCl may shift the δ^{56}Fe values of FeS_x lower by at most 0.02‰, which is insignificant given the analytical error of ±0.08‰. At the highest pyritization extent measured (0.99 for the 'PSG100' experiment at day 7), pyrite-Fe can comprise 25% of the HCl-extractable fraction and may significantly shift the δ^{56}Fe values of FeS_x lower by 0.26‰. We therefore do not consider this datum in our interpretation. Overall, pyrite δ^{56}Fe values are always lower compared to FeS_x, with an average $\Delta^{56}Fe_{pyrite\text{-}FeSx}$ of -0.51 ± 0.22‰ for the entire dataset ($n = 19$). The average isotopic fractionations for all five experiments are identical to one another within error (Table 1). With increasing pyritization extent, pyrite δ^{56}Fe values approach the initial δ^{56}Fe of FeS_x. The isotopic evolution more closely follows closed-system equilibrium behavior than Rayleigh distillation, although neither type of behaviors can completely explain the data; this is especially true at low pyritization extents (Fig. 3c).

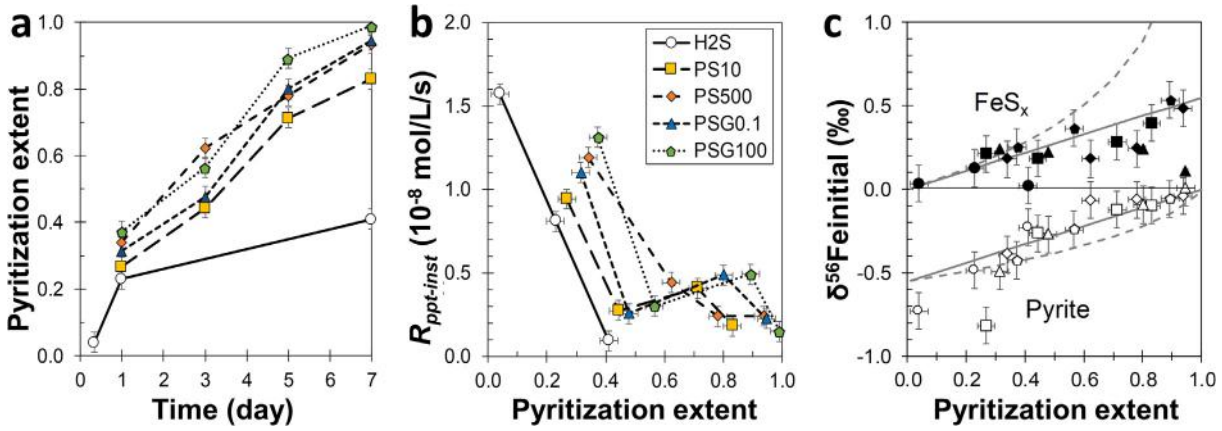

Fig. 3. Changes in precipitation rate and Fe isotopic composition over the course of pyrite precipitation. Symbols specific to each experiment are shown in panel b. (a) Pyritization extent as a function of time. (b) Instantaneous pyrite precipitation rate ($R_{ppt\text{-}inst}$) as a function of pyritization extent. (c) The δ^{56}Fe values of pyrite (white symbols) and FeS_x (black symbols) relative to the initial Fe source as a function of pyritization extent. The isotopic evolution is more consistent with closed-system equilibrium behavior (solid lines) than Rayleigh distillation (dashed lines), assuming an isotopic fractionation factor of 0.99945.

4. DISCUSSION

4.1. Similarities in the isotopic composition of pyrite precipitated via the H_2S and polysulfide pathways

In our study, we seek to determine the Fe isotopic fractionation associated with the H_2S and polysulfide pathways for pyrite precipitation. Differences in sulfur speciation within these pathways can conceivably alter the $\delta^{56}Fe$ of FeS_{aq} (its isotopic composition can vary by ~1‰ as controlled by isotopic exchange with Fe^{2+} and $FeHS^+$ and their relative abundances; Fujii et al., 2014), which may then be reflected in the resulting pyrite. Additional differences in isotopic fractionation can arise due to the relative importance of nucleation compared to growth in the experiments. Pyrite nucleation is typically rate-limiting and proceeds through both the H_2S and polysulfide pathways, while pyrite growth is typically fast and dominated by the polysulfide pathway (Rickard and Luther, 2007). In our 'H_2S' experiment, the pyritization extent is limited to 0.41 after 7 days of incubation, which reflects the maximum pyrite that could be formed via nucleation and growth mediated by the H_2S pathway. This threshold can be attributed to the limited availability of H_2S_{aq}, which constitutes only half of the total aqueous sulfide at any point in the experiment ($H_2S_{aq} \leftrightarrow HS^-$; log $K_{eq} \approx 7$). The polysulfide pathway could operate at later stages in the 'H_2S' experiment owing to polysulfide formation on the surfaces of pre-formed pyrite (Harmandas et al., 1998), but the effects are likely minimal. In the 'PS' and 'PSG' experiments, the initial precipitation rates and final pyritization extents are higher than in the 'H_2S' experiment. The addition of S(0) provides aqueous polysulfide (Eq. (3)) and active surface areas that increase both the nucleation and growth rates of pyrite (e.g., Schoonen and Barnes, 1991). Thus, our experimental systems are dominated by either the H_2S or polysulfide pathway, but in no experiments are the pathways in the strictest sense completely separated from one another. This condition likely holds true for more complex natural systems as well. Considering these factors, we find negligible differences in the apparent isotopic fractionation between experiments dominated by the H_2S pathway versus the polysulfide pathway (i.e., 'H_2S' versus 'PS10' and 'PS500' experiments). The average apparent isotopic fractionation ($\Delta^{56}Fe_{pyrite\text{-}FeSx}$) determined for each pathway is identical within error, though in general the isotopic fractionation is larger in the early stages of precipitation compared to later stages (Fig. 3c). This could imply a slightly larger isotopic fractionation associated with nucleation compared to growth. Overall however, there are no clear differences in the isotopic fractionation associated with pyrite precipitation between the two pathways.

In two of our experiments ('PSG0.1' and 'PSG100'), greigite is produced alongside pyrite when both aqueous molybdenum and S(0) are present. There is no direct evidence from our experiments that pyrite formed via greigite as an intermediate, although previous studies have shown that this reaction is possible (e.g., Sweeney and Kaplan, 1973; Wilkin and Barnes, 1997; Benning et al., 2000). The pyrite in these experiments may therefore be a mixture of pyrite precipitated either (i) directly from a $FeS/Fe(II)_{aq}$ mixture or (ii) via a greigite intermediate (that itself was initially formed from a $FeS/Fe(II)_{aq}$ mixture), resulting in bulk pyrite with isotopic compositions that depend on the relative importance, and the endmember pyrite $\delta^{56}Fe$, of each pathway (Electronic Annex (EA) section A; Fig. EA-4). The isotopic fractionation associated with greigite precipitation and recrystallization of greigite to pyrite may modify pyrite $\delta^{56}Fe$ in a complex and interrelated manner. Despite this, we have found no systematic or overt difference in the apparent isotopic fractionation when greigite is present (average $= -0.50 \pm 0.21$‰ for 'PSG0.1' and 'PSG100') versus when it is absent (average $= -0.50 \pm 0.22$‰ for 'PS10' and 'PS500'). Therefore, at least in our study, there is little evidence that greigite formation impacts pyrite $\delta^{56}Fe$ values.

4.2. Isotopic fractionation associated with pyrite precipitation as a function of the rate of precipitation and isotopic exchange

Another main goal of this study is to evaluate the effects of precipitation rate and isotopic exchange on the isotopic fractionation associated with pyrite precipitation. Notably, the average $\Delta^{56}Fe_{pyrite\text{-}FeSx}$ of -0.51 ± 0.22‰ determined in this study is smaller than the average value of -2.28 ± 0.39‰ observed by Guilbaud et al. (2011b) for the H_2S pathway. Both studies have comparable experimental design in terms of temperature and pH but differ drastically in terms of the precipitation rates. Guilbaud et al. (2011b) utilized 500 mM freeze-dried FeS as the starting reactant and reacted this material with excess sulfide, thus allowing for complete pyritization at precipitation rates of 10^{-5}–10^{-6} mol/L/s. In comparison, we reacted 3 mM Fe (II) with sulfide at a S/Fe ratio of 2:1 in our 'H_2S' experiment and achieved incomplete pyritization at precipitation rates of 10^{-8}–10^{-9} mol/L/s. Differences in the S/Fe ratios cannot explain the smaller isotopic fractionation observed in our study, as one expects our experiment to have larger isotopic fractionation due to incomplete pyritization. Instead, we consider three explanations for the variation of $\Delta^{56}Fe_{pyrite\text{-}FeSx}$ as a function of reaction rates: (i) a rate-dependent KIE, (ii) differential expression of the KIE and EIE as a function of the relative precipitation and isotopic exchange rates between pyrite and $Fe(II)_{aq}$, and (iii) variable isotopic exchange rate between FeS and $Fe(II)_{aq}$ in the absence of isotopic exchange between pyrite and Fe $(II)_{aq}$.

4.2.1. A potential rate-dependent KIE associated with pyrite precipitation

One possible explanation for the large difference in $\Delta^{56}Fe_{pyrite\text{-}FeSx}$ is that the KIE varies as a function of the precipitation rate. This hypothesis is tentatively supported by our data: $\Delta^{56}Fe_{pyrite\text{-}FeSx}$ averages -0.75 ± 0.15‰ during the early stages of precipitation associated with higher rates ($R_{ppt\text{-}inst} \geq 0.94 \cdot 10^{-8}$ mol/L/s) and decreases to -0.44 ± 0.18‰ during the latter stages of precipitation associated with lower rates ($R_{ppt\text{-}inst} < 0.94 \cdot 10^{-8}$ mol/L/s). As discussed earlier, this difference could also be attributed

to variation in isotopic fractionation due to early-stage nucleation compared to later-stage growth, and currently it is difficult to distinguish between a rate-dependent KIE and nucleation/growth effects.

To evaluate whether a correlation exists between precipitation rates and $\Delta^{56}Fe_{pyrite\text{-}FeSx}$, we compile all the available experimental data from pyrite precipitation studies (Fig. 4a). Some of these studies differ considerably in terms of the experimental setups (e.g., S/Fe ratios, temperature, pH and initial reactant concentrations) but a first-order comparison is useful for determining if precipitation rate is a primary control on $\Delta^{56}Fe_{pyrite\text{-}FeSx}$. For experiments conducted at temperatures $\leq$80 °C, $\Delta^{56}Fe_{pyrite\text{-}FeSx}$ appears to increase as precipitation rate increases; this relationship is described by:

$$\Delta^{56}Fe_{pyrite-FeSx} = -0.7112(\log R_{ppt-inst})–6.5403;\ R^2 = 0.9982 \quad (9)$$

Meanwhile, experiments at temperatures $\geq$100 °C display smaller $\Delta^{56}Fe_{pyrite\text{-}FeSx}$ values than the 40 °C experiments even though the precipitation rates are comparable. In the experiments at 300 to 350 °C, pyrite undergoes isotopic exchange with $Fe(II)_{aq}$, which shifts pyrite $\delta^{56}Fe$ towards more positive values (Syverson et al., 2013). A similar isotope exchange process could have affected pyrite $\delta^{56}Fe$ in the 100 °C experiment, although isotopic exchange was previously considered negligible at this temperature because of pyrite's low solubility (Guilbaud et al., 2011b). Ultimately, while some of the data are consistent with a rate-dependent KIE, it is clear that this process cannot be the only factor affecting the Fe isotopic fractionation associated with pyrite precipitation (Fig. 4b).

4.2.2. Isotopic exchange between pyrite and $Fe(II)_{aq}$ as an important process affecting the isotopic composition of experimentally-formed pyrite

Alternatively, we consider the case in which the KIE is independent of the precipitation rate, and the observed isotopic variability can be fully explained by the relative expression of the KIE and EIE associated with precipitation (Fig. 4c). In this case, $\Delta^{56}Fe_{pyrite\text{-}FeSx}$ will be controlled by the rate of precipitation relative to isotopic exchange, and the endmember fractionation factor for the KIE (α_{KIE}) (associated with precipitation reaction) and EIE (α_{EIE}) (associated with isotopic exchange reaction between pyrite and $Fe(II)_{aq}$), similar to the surface kinetic/entrapment models proposed in earlier studies (Watson, 2004; Fantle and DePaolo, 2007; DePaolo, 2011).

The rate (R) at which a mineral reacts is generally described by (Maher et al., 2006):

$$R = SA \cdot k \cdot e^{-E_a T} \cdot \beta(a_i) \cdot (1 - IAP/K_{sp}) \quad (10)$$

and is a function of the mineral surface area (SA), the intrinsic rate constant (k; which varies as a function of temperature, T, and the activation energy, E_a), inhibition and catalytic effects ($\beta(\alpha_i)$), and the saturation state (IAP/K_{sp}). Our hypothesis is predicated on the concept that the functional dependencies of isotopic exchange and net precipitation rates are not the same, allowing for variations in the ratio of net precipitation to exchange. For example, net calcite precipitation rate increases primarily with increasing saturation state (e.g., Morse et al., 2007; Van Der Weijden and Van Der Weijden, 2014; Sand et al., 2016), while isotopic exchange rate is expected to depend primarily on temperature (DePaolo, 2011). Therefore, we hypothesize that the EIE is expressed more strongly in experiments in which net precipitation rate is relatively slow compared to the rate of isotopic exchange.

We can quantify the range of net precipitation and isotopic exchange rates over which such a mechanism is effective using a numerical model that simulates the Fe isotopic evolution of FeS, $Fe(II)_{aq}$ (defined as the total aqueous Fe (II) that includes primarily Fe^{2+}, FeS_{aq}, and $FeHS^+$), and pyrite over the course of pyrite precipitation (EA section B). Our model is constructed using the CrunchTope software package (Steefel et al., 2015) and accounts for both

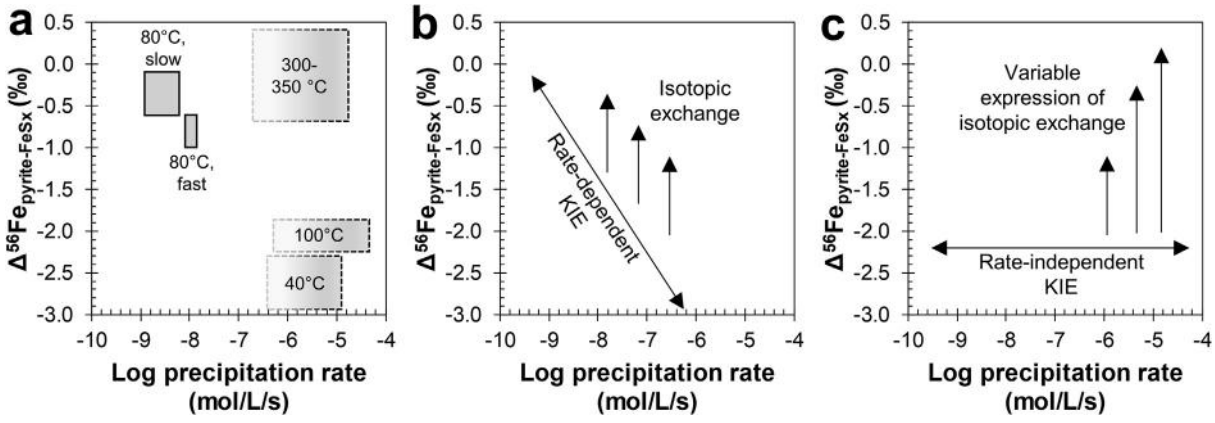

Fig. 4. (a) The apparent isotopic fractionation ($\Delta^{56}Fe_{pyrite\text{-}FeSx}$) associated with pyrite precipitation as a function of instantaneous precipitation rates. Data at 40 °C and 100 °C from Guilbaud et al. (2011b) and data at 300–350 °C from Syverson et al. (2013). Data at 80 °C are from this study and are separated into "fast" and "slow" groups using a threshold rate of $0.94{\cdot}10^{-8}$ mol/L/s. (b) A hypothetical scenario in which $\Delta^{56}Fe_{pyrite\text{-}FeSx}$ values reflect a combination of a rate-dependent kinetic isotope effect (KIE) and variable expression of isotopic exchange between pyrite and $Fe(II)_{aq}$. (c) A hypothetical scenario assuming a rate-independent KIE, in which $\Delta^{56}Fe_{pyrite\text{-}FeSx}$ values reflect solely the variable expression of isotopic exchange as a function of temperature and/or the relative rate of isotopic exchange to precipitation.

equilibrium and kinetic isotope effects. In the model, FeS dissolves to form $Fe(II)_{aq}$, which subsequently precipitates as pyrite (Fig. 5a). Pyrite is permitted to undergo isotopic exchange with $Fe(II)_{aq}$. We assume: (i) a steady state condition, such that the FeS dissolution flux is equal to the pyrite precipitation flux, (ii) that FeS dissolution imparts no isotopic fractionation, (iii) that FeS is in isotopic equilibrium with $Fe(II)_{aq}$ at all times, with no isotopic fractionation between them, (iv) an α_{KIE} of 0.9978 for pyrite precipitation (Guilbaud et al., 2011b), and (v) an α_{EIE} of 1.004 between pyrite and $Fe(II)_{aq}$ (Blanchard et al., 2009; Polyakov and Soultanov, 2011; Syverson et al., 2013).

The modeled pyrite isotopic exchange reaction is:

$$^{54}FeS_2 + {}^{56}Fe(II)_{aq} \leftrightarrow {}^{56}FeS_2 + {}^{54}Fe(II)_{aq} \quad (11)$$

and the rate of isotopic exchange between pyrite and $Fe(II)_{aq}$ (R_{ex}) is assumed to be governed by the expression:

$$R_{ex} = k_{pyrite\_ex}\left(1 - \frac{Q}{Keq}\right) \quad (12)$$

where k_{pyrite_ex} is the rate constant (unit of mol/L/s) and Q and K_{eq} are the reaction quotient and the equilibrium constant, respectively, for the isotopic exchange reaction. It can be shown that K_{eq} is equal to the equilibrium fractionation factor:

$$K_{eq} = \alpha_{EIE} = \frac{[{}^{56}FeS_2][{}^{54}Fe(II)]}{[{}^{54}FeS_2][{}^{56}Fe(II)]} \quad (13)$$

where the symbol "[]" denotes concentration in mol/L. With this formulation, the rate of isotopic exchange slows as the system approaches isotopic equilibrium. In the following simulations, we consider a "zero-order kinetics" scenario in which pyrite precipitation rate (R_{ppt}) is assumed to be constant. This assumption allows us to explore the effect of varying k_{pyrite_ex} relative to R_{ppt} on the Fe isotopic compositions of pyrite. The ratio of k_{pyrite_ex} to R_{ppt} is defined as the unitless parameter W:

$$W = k_{pyrite\_ex}/R_{ppt} \quad (14)$$

where W is a measure of the relative expression of the EIE to the KIE. A higher value of W indicates a greater expression of the EIE compared to the KIE and vice versa.

The simulation results demonstrate that variation in W produces a range of FeS_x and pyrite $\delta^{56}Fe$ values consistent with Rayleigh-like to closed system equilibrium systems (Fig. 5b and c). Significantly, the Fe isotopic evolution for pyrite and FeS_x in experiments at temperatures from 40 to 100 °C can be explained by assuming a rate-independent KIE and by varying W. The extent to which isotopic exchange occurs generally follows the experimental temperature: pyrite precipitated at 40 °C evolves along a Rayleigh distillation trend, consistent with slow/non-existent exchange (upper limit for W of 0.003), while pyrite precipitated at 80 °C and 100 °C display partial isotopic exchange trends ($W = 0.009$–0.027). Pyrite precipitated at 300–350 °C are not considered because of the lack of isotopic data measured across pyritization extents. One outstanding detail is that pyrite precipitated at 100 °C is associated with a lower W value (less expression of EIE) than pyrite precipitated at 80 °C. Nevertheless, the k_{pyrite_ex}

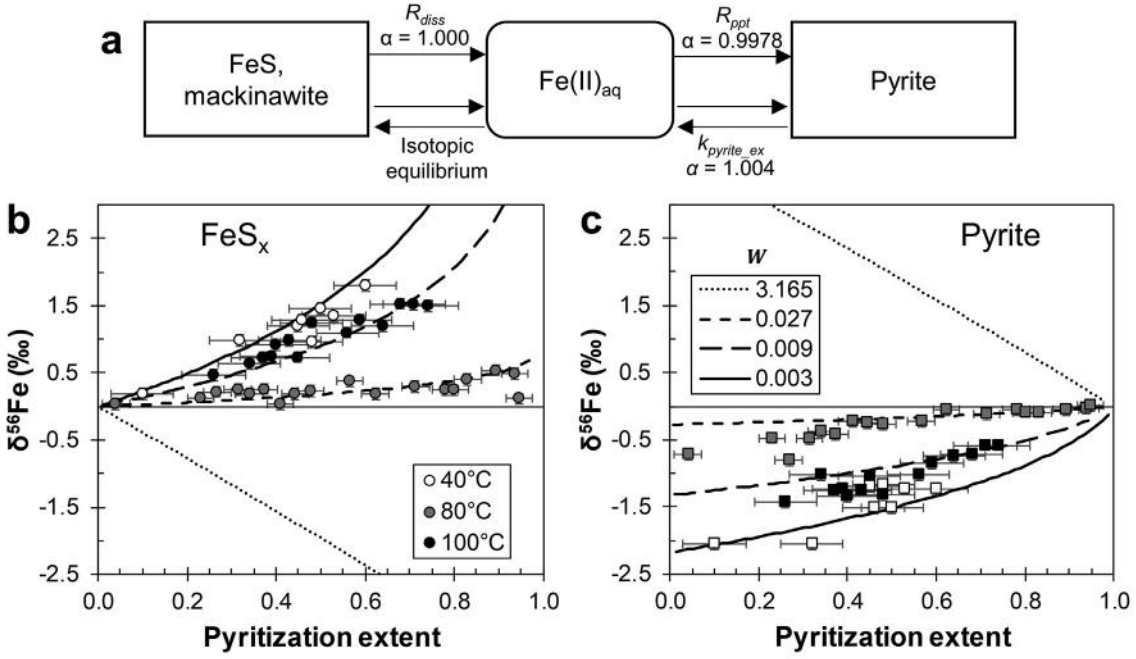

Fig. 5. (a) Schematic of the batch numerical model used to evaluate the effect of variable isotopic exchange rate between pyrite and $Fe(II)_{aq}$ on $\delta^{56}Fe$ values, assuming constant R_{ppt}. (b-c) Simulation results (solid/dashed lines) at variable values of W (defined as k_{pyrite_ex} / R_{ppt}). Symbols denote measured $\delta^{56}Fe$ values of (b) FeS_x and (c) pyrite from experiments at different temperatures (this study, Guilbaud et al.; 2011b). All $\delta^{56}Fe$ values are reported relative to the initial reactant. The isotopic data are consistent with variable extent of isotopic exchange between pyrite and $Fe(II)_{aq}$. Error bars of measured $\delta^{56}Fe$ values are ±0.08‰ and are smaller than the size of the symbols.

value associated with the 100 °C experiments is higher than at 80 °C (Fig. 6), which is consistent with the notion that isotopic exchange rate should increase with temperature. Because W is also dependent on net precipitation rate, it illustrates how fast precipitation rates can obscure the expression of the EIE in experimental systems. This is especially important to keep in mind when one considers that pyrite formed in experiments (this study; Canfield et al., 1998; Harmandas et al., 1998; Rickard et al., 2007; Guilbaud et al., 2011b; Morin et al., 2017; Wan et al., 2017) are often associated with orders of magnitude higher precipitation rates compared to natural settings (Fig. 7). The isotopic composition of sedimentary pyrite may therefore be more strongly affected by isotopic exchange compared to experimentally-formed pyrite.

Overall, the experimental data are consistent with isotopic exchange reactions between pyrite and $Fe(II)_{aq}$ during precipitation, especially in the 100 °C experiments. Isotopic exchange is also consistent with the Fe isotopic evolution of pyrite and FeS_x at 80 °C, although the current simulation poorly reproduces pyrite $\delta^{56}Fe$ values at pyritization extents less than 0.40 and does not exclude the possibility of additional variation caused by either a rate-dependent KIE or nucleation/growth effects. This observation will be discussed further in Section 4.3.

4.2.3. Evaluating isotopic exchange between FeS and $Fe(II)_{aq}$ as an additional cause for variations in pyrite $\delta^{56}Fe$

One major assumption in our simulations is that the mineral FeS and the total $Fe(II)_{aq}$ species are always in isotopic equilibrium, with no isotopic fractionation between these two phases. Importantly, Guilbaud et al. (2011b) previously argued that continuous isotopic exchange between FeS and $Fe(II)_{aq}$ in their 100 °C experiments can modify the isotopic evolution of the system, yielding an apparent closed system equilibrium trend between pyrite and FeS_x. It is recognized however that at low temperatures (2–35 °C), both the time to attain equilibrium and the equilibrium fractionation factor ($\alpha_{FeS\text{-}Fe(II)}$) can depend on the speciation of $Fe(II)_{aq}$ (Butler et al., 2005; Guilbaud et al., 2010; Wu et al., 2012). A state of isotopic disequilibrium between FeS and $Fe(II)_{aq}$ can persist for a few weeks. It is therefore worth exploring how uncertainties in (i) $\alpha_{FeS\text{-}Fe(II)}$ and (ii) the rate of isotopic exchange between FeS and $Fe(II)_{aq}$ might affect $\Delta^{56}Fe_{pyrite\text{-}FeSx}$ values in experimental systems.

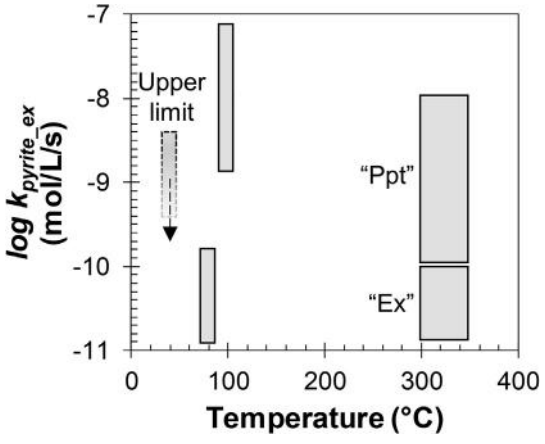

Fig. 6. Estimates of k_{pyrite_ex} values from simulations of experiments. The estimate at 40 °C is given as an upper limit as there is no clear evidence for isotopic exchange in that experiment. "Ppt" and 'Ex" correspond to the precipitation and partial exchange experiments of Syverson et al. (2013), respectively.

Predicting the effects of variable $\alpha_{FeS\text{-}Fe(II)}$ on $\Delta^{56}Fe_{pyrite\text{-}FeSx}$ is logically straightforward. If we assume an $\alpha_{FeS\text{-}Fe(II)}$ of 1.0006 (for systems dominated by FeS_{aq} and $FeHS^+$) compared to 1.0000 (for systems dominated by Fe^{2+}) (see review by Wu et al., 2012), the isotopic composition of $Fe(II)_{aq}$ shifts lower by 0.6‰ at equilibrium, which then causes pyrite $\delta^{56}Fe$ to shifts lower by the same amount (see Fig. 10 and compare simulation 'A' to simulation 'D'). Therefore, $\Delta^{56}Fe_{pyrite\text{-}FeSx}$ appears to be larger by 0.6‰ since the isotopic composition of FeS_x is dominated by the solid FeS. Taking into account that the magnitude of the equilibrium fractionation factor between FeS and $Fe(II)_{aq}$ should decrease with increasing temperature (Polyakov and Soultanov, 2011), this process may partially contribute to the apparent relationship of $\Delta^{56}Fe_{pyrite\text{-}FeSx}$ with temperature as noted earlier (Fig. 1), but it should cause no more than 0.6‰ variation. Therefore, this process cannot account for the >1.5‰ variation in $\Delta^{56}Fe_{pyrite\text{-}FeSx}$ values observed across experiments.

A second possibility is that variation in the rate of isotopic exchange between FeS and $Fe(II)_{aq}$ can modify $\Delta^{56}Fe_{pyrite\text{-}FeSx}$values. This effect can be illustrated using a model that has the capability to vary the rate of isotopic exchange between FeS and $Fe(II)_{aq}$ relative to the rate of pyrite precipitation (EA section C). Isotopic exchange between pyrite and $Fe(II)_{aq}$ is not permitted in this model (Fig. 8a). The simulation results indicate significant variations in the isotopic compositions of FeS, $Fe(II)_{aq}$, and pyrite when the relative rate of isotopic exchange between FeS and $Fe(II)_{aq}$ to pyrite precipitation is modified (Fig. 8). At slow pyrite precipitation rates (or fast FeS-$Fe(II)_{aq}$ isotopic exchange rates), FeS and $Fe(II)_{aq}$ behave as a single component that is isotopically distilled at the same rate, resulting in an overall system that evolves along a Rayleigh distillation trend. This contradicts the findings of Guilbaud et al. (2011b), who argued that an apparent equilibrium trend between pyrite and FeS_x results when FeS and $Fe(II)_{aq}$ are in isotopic equilibrium.

With increasing pyrite precipitation rates (and slower relative FeS-$Fe(II)_{aq}$ isotopic exchange rates), FeS and Fe $(II)_{aq}$ behave increasingly as two separate components (Fig. 8b and c). The isotopic composition of $Fe(II)_{aq}$ (which represents a small fraction of Fe in the total system) is considerably distilled while the isotopic composition of FeS can remain relatively unaffected until the later stages of pyritization. Meanwhile, pyrite $\delta^{56}Fe$ shifts towards higher values following the evolution of its primary $Fe(II)_{aq}$ source, leading to a smaller $\Delta^{56}Fe_{pyrite\text{-}FeSx}$ a since the $\delta^{56}Fe$ of FeS_x is largely controlled by FeS (Fig. 8d and e). This exercise therefore illustrates how variable rates of isotopic exchange between FeS and $Fe(II)_{aq}$ can cause large variations in the apparent isotopic fractionation associated with pyrite precipitation.

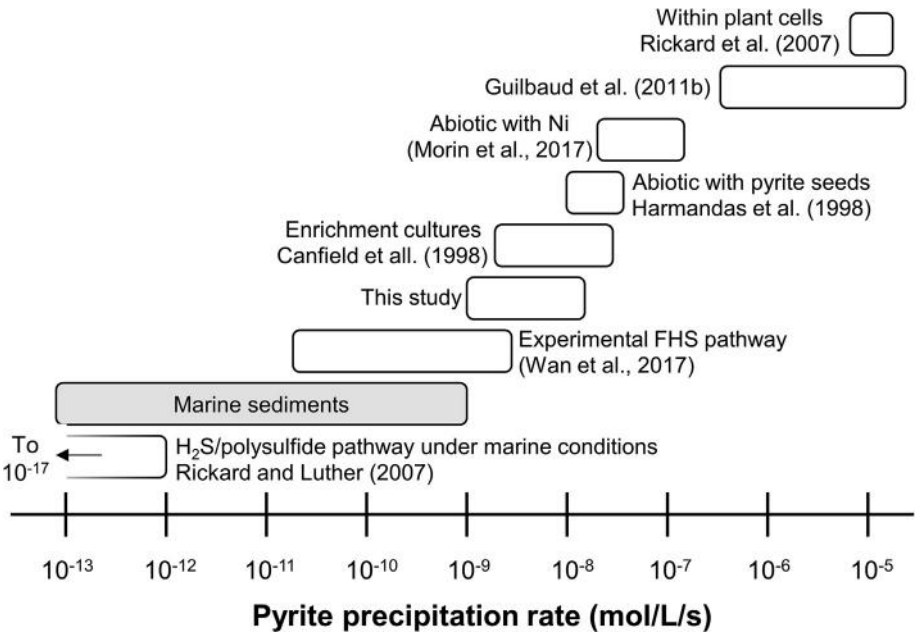

Fig. 7. Compiled pyrite precipitation rates from marine sediments (gray) and experiments (white).

With respect to the experimental data, the Rayleigh distillation trend observed for the 40 °C experiment suggests that FeS and $Fe(II)_{aq}$ are in isotopic equilibrium at this temperature. Therefore, it is likely that these two components are also in isotopic equilibrium in the 80 °C and 100 °C experiments. Thus, variations in the rate of isotopic exchange between FeS and $Fe(II)_{aq}$ cannot account for the difference in $\Delta^{56}Fe_{pyrite\text{-}FeSx}$ between experiments. This is supported by the observations that the evolution of $\Delta^{56}Fe_{pyrite\text{-}FeSx}$ in the experiments is largely inconsistent with simulations employing different rates of isotopic exchange between FeS and $Fe(II)_{aq}$ (Fig. 8e). Hence, isotopic exchange between pyrite and $Fe(II)_{aq}$ remains necessary to explain the experimental data.

4.3. Parameters affecting the isotopic exchange rate between pyrite and $Fe(II)_{aq}$

The rate of isotopic exchange between a mineral (e.g., pyrite) and a fluid (e.g., $Fe(II)_{aq}$) can be affected by several parameters including particle size and aggregation state (which affects the mineral's surface area to volume ratio and the fraction of mineral that is exchangeable), the fluid-to-mineral mass ratio, and temperature (e.g., Maher et al., 2004; Fantle and DePaolo, 2007; Guilbaud et al., 2010; DePaolo, 2011; Gorski and Fantle, 2017). Consequently, the rate law that we assumed for the isotopic exchange reaction (Eq. (12)) is simplified, with k_{pyrite_ex} acting as an effective rate constant that folds into it the parameters discussed above. Below, we describe additional modeling exercises that allow us some insight into the relationship between the aforementioned parameters and the isotopic exchange rate between pyrite and $Fe(II)_{aq}$.

4.3.1. Inferred effect of particle size on isotopic exchange rate

As stated previously, the $\delta^{56}Fe$ values of pyrite at pyritization extents <0.40 in our 80 °C experiments are poorly reproduced by a zero-order kinetics simulation (Fig. 5c); attempts at optimizing the fit to the pyrite data creates a poorer fit to the FeS_x $\delta^{56}Fe$ values at pyritization extents >0.65. We therefore consider if a better fit to the overall data can be obtained if we consider temporal changes in R_{ppt} and k_{pyrite_ex} over the course of precipitation.

First, the rate for pyrite precipitation in our simulation is modified to follow a first-order kinetics rate law with respect to the FeS concentration (EA section D) in order to mimic the decrease in precipitation rate over the course of precipitation (compare Figs. 9a and 3b). If we assume a constant k_{pyrite_ex}, this simulation reproduces the experimental data particularly well up to pyritization extents of ~0.70 but grossly overestimates the extent of exchange at pyritization extents >0.70 (Fig. 9b). A better fit to the data can be obtained by systematically decreasing k_{pyrite_ex} in a stepwise manner (Fig. 9c). We find that at least a 3-step decrease of k_{pyrite_ex} (a total decrease of about an order of magnitude) is required to reproduce the experimental data (Fig. 9c). The $\delta^{56}Fe$ values of FeS_x at high pyritization extents are particularly sensitive to the simulation parameters and serve as the primary constraints on k_{pyrite_ex}. The simulations therefore imply that k_{pyrite_ex} must decrease over the course of precipitation.

The decrease in k_{pyrite_ex} is best explained by an increase in pyrite particle size over time, resulting in a lower mineral surface area to volume ratio. Previous synthesis experiments performed at comparable pH, temperature, and/or reactant concentrations have shown that pyrite particle size increases over time due to either mineral growth or

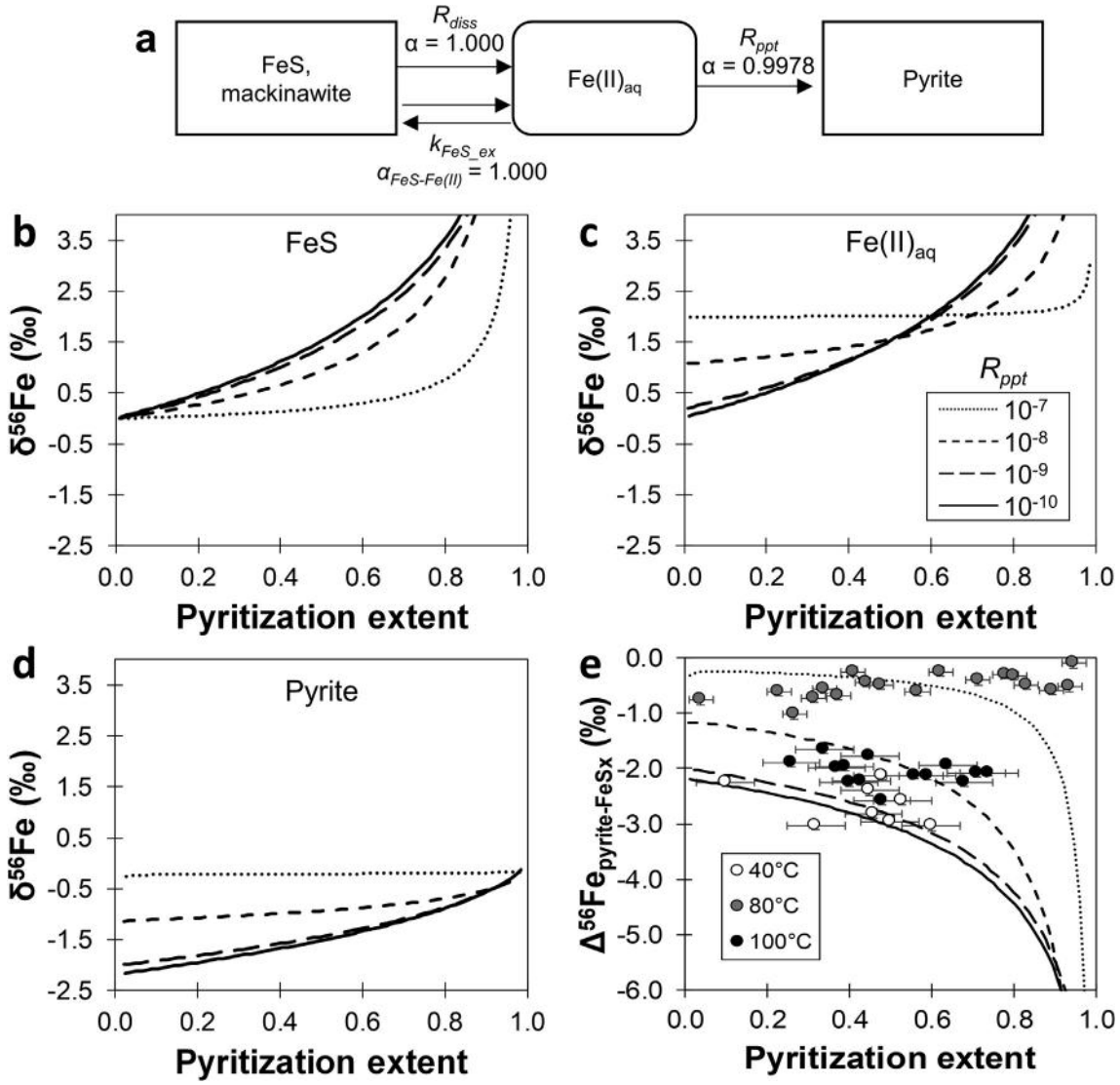

Fig. 8. (a) Schematic of the batch numerical model used to evaluate the effect of variable isotopic exchange rate between FeS and $Fe(II)_{aq}$ on the isotopic evolution of the system. The isotopic exchange rate constant (k_{FeS_ex}) is assumed to be the same for all simulations, with a value that is pre-determined from fitting simulations to data collected from low-temperature exchange experiments (EA section C). The pyrite precipitation rate (R_{ppt}) is varied across the simulation (legends in panel c). Higher R_{ppt} indicates faster precipitation rate relative to isotopic exchange between FeS and $Fe(II)_{aq}$. (b–d) The $\delta^{56}Fe$ values for pyrite, $Fe(II)_{aq}$, and FeS as a function of pyritization extent. (e) The apparent isotopic fractionation between pyrite and FeS_x across pyritization extent compared to experimental data at temperatures of 40–100 °C.

aggregation (Wilkin and Barnes, 1996; Rickard, 1997; Lan and Butler, 2014). Other parameters that can affect isotopic exchange rate in our experiments are either invariant (i.e., temperature) or relatively constant (i.e., fluid-to-mineral ratio). In the latter case, the mass of $Fe(II)_{aq}$ relative to pyrite is always small (except at the earliest stage of the experiment), and a steady-state condition during precipitation is supported when one considers the measured pyrite precipitation rates and assumes FeS dissolution rates following the rate law of Pankow and Morgan (1979).

It is important to note that the isotopic trend in the 80 °C experiment cannot be explained as a consequence of a rate-dependent KIE in the absence of isotopic exchange between pyrite and $Fe(II)_{aq}$ (Fig. 9d; EA section E). A better fit can be obtained by assuming a stronger dependence of the KIE on precipitation rate (i.e., steeper slope for Eq. (9)). However, Eq. (9) was derived assuming no isotopic exchange for the 80 °C experiments and thus already accounts for the strongest possible dependence of the KIE on precipitation rate. Therefore, within the 80 °C experiments, $\delta^{56}Fe$ variations caused by a rate-dependent KIE are small relative to variations caused by changes in k_{pyrite_ex}. If we consider both rate-dependent KIE and isotopic exchange occurring at the same time, the values of k_{pyrite_ex} required to reproduce the data decrease compared to a rate-independent KIE scenario, but it does not change

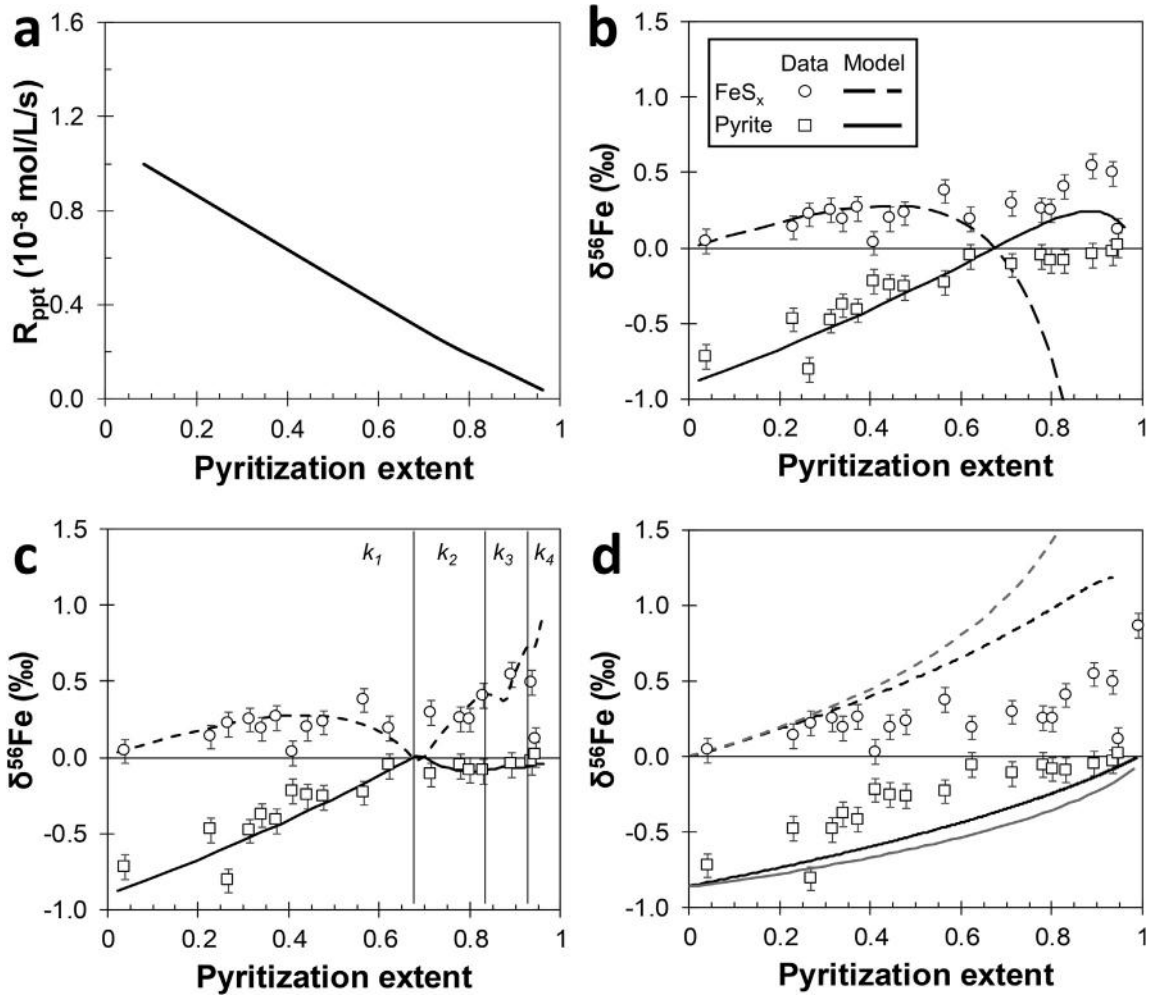

Fig. 9. Results for the first-order kinetics simulation. (a) The change in precipitation rate with pyritization extent. (b) The δ^{56}Fe evolution of FeS_x and pyrite (solid/dashed lines from model) assuming a constant k_{pyrite_ex} of $15.85{\cdot}10^{-11}$ mol/L/s. Measured δ^{56}Fe values from the 80 °C experiments are represented as circle or square symbols. This simulation overestimates isotopic exchange at pyritization extents >0.70. (c) The δ^{56}Fe evolution of FeS_x and pyrite assuming a 3-step decrease in k_{pyrite_ex} ($k_1 = 15.85$, $k_2 = 4.76$, $k_3 = 1.59$, $k_4 = 0.95{\cdot}10^{-11}$ mol/L/s). Vertical lines delineate the zones corresponding to the chosen value of k_{pyrite_ex}. This simulation agrees fairly well with the experimental data. (d) The δ^{56}Fe evolution of FeS_x and pyrite assuming no isotopic exchange and a rate-dependent KIE (black lines). Gray lines represent simulation results assuming a constant α_{KIE} of 0.99914 (equal to the initial rate-dependent α_{KIE}) for comparison. This simulation fails to reproduce the isotopic trend.

the requirement that k_{pyrite_ex} must decrease as the reaction progresses to avoid overestimating the extent of isotopic exchange.

4.3.2. Extrapolating the isotopic exchange rate to low temperature

The recognition that pyrite isotopically exchanges at temperatures below 100 °C leads us to consider whether isotopic exchange is an important control on sedimentary pyrite δ^{56}Fe values. If isotopic exchange rate correlates with temperature, it may be reasonable to extrapolate high temperature experimental data to constrain k_{pyrite_ex} at lower temperatures. From the simulations, we can estimate values for k_{pyrite_ex} at 40 °C and 100 °C by multiplying the range of W that best characterizes each experiment (Fig. 5) by their respective range of R_{ppt} (Fig. 4). The k_{pyrite_ex} value at 40 °C is given as an upper limit as there is no obvious isotopic exchange in that experiment. The value for k_{pyrite_ex} at 80 °C is obtained from the first-order kinetics simulation, with the recognition that the actual values may be lower if we consider a rate-dependent KIE. We also extend the model to constrain k_{pyrite_ex} from Syverson et al.'s (2013) "precipitation" and "partial exchange" experiments at 300–350 °C, which result in k_{pyrite_ex} estimates of 10^{-8}–10^{-10} and 10^{-10}–10^{-11} mol/L/s, respectively (EA section F; Fig. EA-5 and EA-6). Higher k_{pyrite_ex} estimates for the "precipitation" experiments are in agreement with the hypothesis that the rate decreases with increasing particle size; the "precipitation" experiments yielded ~1 μm sized pyrite grains while the partial exchange experiments utilized well-crystallized pyrite grains a few tenths of micron in size.

Intriguingly, there is no systematic correlation between temperature and k_{pyrite_ex} (Fig. 6). Comparisons across these multiple studies are not straightforward because of the differences in experimental setups that include S/Fe ratios, solution matrix, pyrite grain size, particle aggregation, and pH. For example, the 300–350 °C experiments utilized a more acidic medium (pH = 1.5) than the near-neutral pH employed in the other experiments. Solution pH is a major control on Fe speciation, with lower pH associated with the prevalence of aqueous Fe^{2+} and near-neutral pH associated with the dominance of aqueous Fe-sulfide complexes in the presence of excess sulfide (Rickard and Luther, 2007). All of these variations may affect the apparent isotopic exchange rate between $Fe(II)_{aq}$ and pyrite. A self-consistent set of experiments performed at different temperatures is needed to fully investigate the relationship between k_{pyrite_ex} and temperature.

Discounting the acidic 300–350 °C experiments and the 40 °C experiment where no isotopic exchange is evident, we observe a decrease in k_{pyrite_ex} from 100 to 80 °C. We can extrapolate from these datasets to derive k_{pyrite_ex} values of 10^{-19}–10^{-18} mol/L/s at temperatures of 4–25 °C. It is difficult to assign confidence for this range in k_{pyrite_ex} because essentially only two data points are available for extrapolation. At this point, it is just as reasonable to assume that a k_{pyrite_ex} of 10^{-11} mol/L/s (consistent with the lowest k_{pyrite} estimates in experiments) represents the upper limit for the isotopic exchange reaction at low temperatures. Hence, current estimates for k_{pyrite_ex} that are applicable to sedimentary settings range from 10^{-19} to 10^{-11} mol/L/s. In the next section, we will illustrate how variations in k_{pyrite_ex} across this range can affect sedimentary pyrite δ^{56}Fe.

4.4. Constraining the range of sedimentary pyrite δ^{56}Fe values in the presence of isotopic exchange reactions

The degree to which isotopic exchange can affect sedimentary pyrite δ^{56}Fe can be explored by adjusting our model inputs to better reflect sedimentary conditions. It is first useful to discuss uncertainties in the model inputs, which include (i) the range in values of maximum α_{KIE} and α_{EIE}, (ii) the range in values of W, which is a function of the pyrite precipitation rate and k_{pyrite_ex}, and (iii) the presence of co-existing Fe-sulfide phases that can affect pyrite precipitation pathway and/or the isotopic composition of $Fe(II)_{aq}$ from which pyrite forms.

4.4.1. Constraints on the maximum isotopic fractionation factors associated with the kinetic (α_{KIE}) and equilibrium isotope effects (α_{EIE})

In all of the previous simulations, we have assumed a maximum α_{KIE} value of 0.9978 based on the results of Guilbaud et al. (2011b). However, this value is constrained by high temperature experiments in which exchange might have occurred. Recent work in the Black Sea suggests an even larger isotopic fractionation factor of −2.75‰ ($\alpha_{KIE} = 0.9925$) associated with pyrite precipitation from $Fe(II)_{aq}$ in an euxinic water column (Rolison et al., 2018). However, it is important to note that this α_{KIE} is derived solely from isotopic measurements of $Fe(II)_{aq}$ and assumes that all of the $Fe(II)_{aq}$ in the euxinic water column is incorporated into pyrite. This assumption is yet to be evaluated. The possibility of rate- and temperature-dependent effects also contribute to uncertainty in the maximum α_{KIE} value.

It is also not clear what the value of α_{EIE} is in low temperature systems, as it has not been determined experimentally. Prediction from density functional theory, Mössbauer and inelastic nuclear resonant X-ray scattering data, and extrapolation from high temperature experiments suggest a range in α_{EIE} values between 1.0035 and 1.0070 at 5–25 °C (Blanchard et al., 2009; Rustad et al., 2010; Polyakov and Soultanov, 2011; Syverson et al., 2013).

Simulations performed at variable W values (assuming constant precipitation rates) indicate that the degree to which uncertainties in α_{KIE} and α_{EIE} affect pyrite δ^{56}Fe largely depends on the W regime (Fig. 10). Varying α_{KIE} over its current uncertainty range translates to a maximum ~0.5‰ variation in pyrite δ^{56}Fe, with the largest variations observed when $W \leq 0.01$ (low exchange regime). Meanwhile, varying α_{EIE} over its uncertainty range can cause as much as 3.5‰ variation in pyrite δ^{56}Fe, with the largest variations observed when $W \geq 0.1$ (high exchange regime). In partial exchange regime ($W = 0.01$–0.1), pyrite δ^{56}Fe values are more sensitive to changes in α_{EIE} due to the larger uncertainties in α_{EIE} compared to α_{KIE}.

4.4.2. Constraints on W values and the importance of KIE relative to EIE in sedimentary settings

As discussed previously, the δ^{56}Fe values of pyrite are significantly impacted by the W values associated with precipitation. At high values of W, the expressed isotopic fractionation will be dominated by the EIE, generating pyrite with positive δ^{56}Fe. At low values of W, the expressed isotopic fractionation will be dominated by the KIE, generating pyrite with negative δ^{56}Fe. We have therefore attempted to constrain W for sedimentary pyrite by compiling literature data for precipitation rates and combining it with our estimates of k_{pyrite_ex}.

Pyrite precipitation rates in marine sediments are found to vary by about 4 orders of magnitude, ranging from 10^{-9} to 10^{-13} mol/L/s (Fig. 7). These rates are calculated based on measurements of radioactive sulfur ($^{35}SO_4$) that are incorporated into pyrite over a given time period within a given sediment depth interval (Lein, 1983; Howarth and Jorgensen, 1984; Thode-Andersen and Jørgensen, 1989; Fossing, 1990; Lin and Morse, 1991; Lin et al., 2000; Lin et al., 2002). This method can overestimate pyrite precipitation rates due to unaccounted for ^{35}S exchange between dissolved sulfur pools, S(0) adsorbed on pyrite grains, and pre-existing pyrite (Fossing et al., 1992). This method can also underestimate precipitation rates due to oxidative loss of pyrite, especially near the sediment-water interface (Lin et al., 2000; Lin et al., 2002). The error due to these effects is unconstrained but is unlikely to cause the four orders of magnitude variation in the measured rates.

Assuming a k_{pyrite_ex} range of 10^{-19}–10^{-11} mol/L/s, sedimentary pyrite precipitation is thus associated with W values that range from <0.01 to 100. The effect of varying W over this large range, coupled to uncertainties in α_{KIE} and

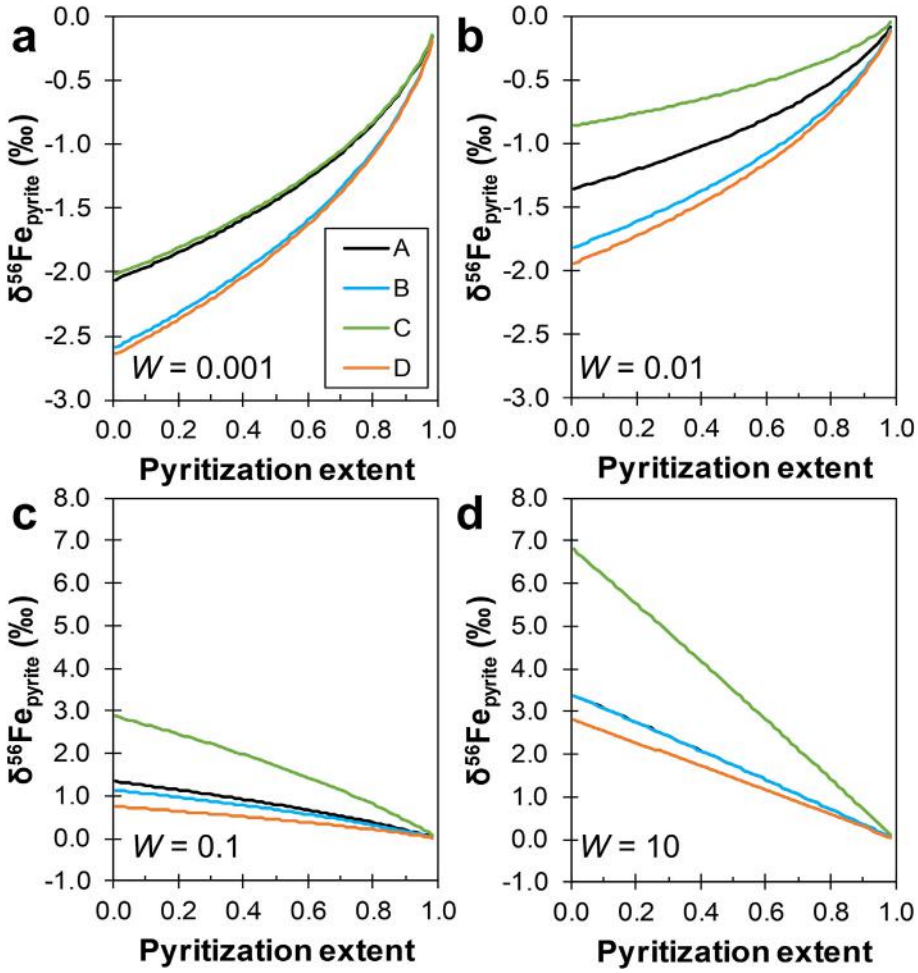

Fig. 10. Sensitivity analysis of the zero-order kinetic simulations to variable values of W, α_{KIE} α_{EIE}, and $\alpha_{FeS\text{-}Fe(II)}$. Each panel indicate results of simulations performed at a constant W value. Within each panel, four simulation results are presented: condition A ($\alpha_{KIE} = 0.99780$, $\alpha_{EIE} = 1.0035$, $\alpha_{FeS\text{-}Fe(II)} = 1.0000$), B (same as "A" except $\alpha_{KIE} = 0.99725$), C (same as "A" except $\alpha_{EIE} = 1.0070$), and D (same as "A" except $\alpha_{FeS\text{-}Fe(II)} = 1.0006$). Note the different y-axis for panels a and b versus panels c and d.

α_{EIE}, results in pyrite with $\delta^{56}Fe$ values that range from $\sim -3‰$ to $\geq 4‰$ (Fig. 10), which spans almost the entire range of natural pyrite $\delta^{56}Fe$ values. Of course, the actual isotopic fractionation associated with sedimentary pyrite precipitation depends on k_{pyrite_ex}, which is highly uncertain at low temperature. Nonetheless, isotopic exchange will only be irrelevant for sedimentary pyrite precipitation if the current upper limit for k_{pyrite_ex} is overestimated by five orders of magnitude (i.e., k_{pyrite_ex} must be less than 10^{-16} mol/L/s).

We can further constrain the importance of the KIE relative to the EIE on sedimentary pyrite precipitation based on the apparent isotopic fractionation observed between pyrite and Fe(II)-containing components in low temperature environments. In modern marine sediments, bulk pyrite displays an apparent isotopic fractionation of −1.9 to +2.0‰ relative to HCl-extractable Fe(II) (Severmann et al., 2006; Fehr et al., 2010; Scholz et al., 2014). Most of the positive values originated from samples with low pyritization extents, wherein the isotopic compositions of the Fe(II)-containing components are affected by intensive Fe redox cycling (Severmann et al., 2006). Disregarding samples at low pyritization extents (<0.2), $\Delta^{56}Fe_{pyrite\text{-}Fe(HCl)}$ tends towards negative values with a range of −1.9 to +0.5‰. We interpret this isotopic range to reflect the combined effects of variation in pyritization extent, precipitation pathway, and the higher expression of KIE compared to EIE as modulated by precipitation rates. In comparison, limited isotopic fractionation is inferred for pyrite precipitation in the ferruginous water column of Lake Pavin (Busigny et al., 2014), consistent with a higher degree of isotopic exchange between $Fe(II)_{aq}$ and pyrite during precipitation in an Fe(II)-rich environment. Overall, the observations indicate that KIE is preferentially expressed over EIE during pyrite precipitation in typical modern marine sediments but does not rule out the importance of isotopic exchange reactions in low temperature environments.

4.4.3. Impact of co-existing Fe-sulfide phases on sedimentary pyrite $\delta^{56}Fe$

The presence of other Fe-sulfide phases such as FeS and greigite within marine sediments can also play a role in controlling sedimentary pyrite $\delta^{56}Fe$. In particular, FeS can be

formed rapidly by the reaction of $Fe(II)_{aq}$ with sulfide, leading to pervasively low pore fluid concentrations of $Fe(II)_{aq}$ (~10 μM in chemical equilibrium with FeS; Rickard, 2006; Rickard and Luther, 2007). As discussed earlier, the rate of isotopic exchange between FeS and $Fe(II)_{aq}$ (relative to pyrite precipitation) may play a large part in determining the isotopic composition of pyrite. However, at rates relevant to marine sediments ($R_{ppt} \leq 10^{-9}$ mol/L/s and $k_{FeS\_ex} = 6.3{\cdot}10^{-10}$ mol/L/s; EA section C; Fig. EA-5), this process may only cause as much as ~0.2‰ variation in pyrite δ^{56}Fe values (Fig. 8).

Greigite is a relatively rare Fe-sulfide phase in marine sediments (Schoonen, 2004; Rickard and Morse, 2005), although some studies suggest that the abundant, naturally-occurring framboidal pyrite can only occur through recrystallization of magnetically-aggregated greigite (Sweeney and Kaplan, 1973; Wilkin and Barnes, 1997; but see Butler and Rickard, 2000 for an alternative interpretation). Depending on the fraction of pyrite that is formed via a greigite intermediate and the fractionation factor associated with greigite formation (both of which are underconstrained), pyrite δ^{56}Fe may be significantly different compared to the case in which greigite is absent (EA section A; Fig. EA-4). In our experiments however, there is no evidence that greigite formation impacted the isotopic fractionation associated with pyrite precipitation. We therefore conclude that sedimentary pyrite δ^{56}Fe is largely a function of the *W* values associated with pyrite precipitation rather than competing effects of other Fe-sulfide phases.

4.5. Implications for interpretations of Earth's redox evolution based on sedimentary pyrite δ^{56}Fe

Sedimentary pyrite precipitation and burial is arguably the most important process for the removal of reduced iron and sulfur from the ocean. This process is mediated by microbial Fe and sulfate reduction in low temperature systems and is linked to the exogenic cycle of oxygen in the Earth's atmosphere via reaction of reduced Fe and S species with oxygen (e.g., Berner, 1984; Canfield, 2005; Johnston et al., 2009). The rate of pyrite precipitation and burial also relates directly to the transition from the anoxic early Earth to the modern oxygen-rich world observed today. Sedimentary pyrite δ^{56}Fe can therefore reflect the evolution of Earth's surface redox state and microbial life over geological time scales.

In this study, we have constrained the degree to which isotopic exchange can affect pyrite δ^{56}Fe, resulting in a novel framework for interpreting pyrite-based Fe isotope records based on the relative expression of the KIE and EIE associated with pyrite precipitation from $Fe(II)_{aq}$ under different environmental conditions. In the following sections, we discuss the implications of our findings from three different viewpoints: post-precipitation alteration of pyrite δ^{56}Fe, microscale pyrite δ^{56}Fe variations, and the negative excursion of bulk pyrite δ^{56}Fe across the Great Oxidation Event.

4.5.1. Post-precipitation alteration of pyrite δ^{56}Fe

After initial pyrite precipitation, additional isotopic exchange between pyrite and residual $Fe(II)_{aq}$ may shift pyrite δ^{56}Fe towards more positive values, leading to δ^{56}Fe values that reflect diagenesis rather than the primary environment during precipitation. This may be especially relevant to pyrite precipitated in a ferrous Archean ocean, with a purported Fe concentration that is much higher (~200 μM) than the modern ocean (<10 nM; e.g., Ohmoto et al., 2014). As discussed previously, the extent of diagenetic alteration depends on the temperature, particle size, fluid-to-mineral mass ratio, and the extent of isotopic disequilibrium (Fantle et al., 2010). The interplay between these parameters is complex and must be considered on a case-by-case basis for pyrite deposited in different settings and even within the same sedimentary unit.

Multiple lines of observations suggest that ancient pyrite retained its primary isotopic composition following precipitation. First, reaction rates between a mineral and a fluid tend to decrease with mineral age (Maher et al., 2004; Fantle and DePaolo, 2007; Gorski and Fantle, 2017), consistent with the observed trends in isotopic exchange rate between pyrite and $Fe(II)_{aq}$ for fresh versus evolved grains in experimental systems (this study; Syverson et al., 2013). This is likely due to the strong dependency of isotopic exchange rate on the availability of reactive surface areas (Reeves and Rothman, 2013). Evolved pyrite grains (e.g., hydrothermal, lignite, and crushed mm-sized sedimentary pyrite) tend to have smaller surface areas than early-formed fine grained sedimentary/synthetic pyrite (Table 2). We therefore expect that older pyrite grains are more resistant to isotopic alteration due to the decrease in the surface area-to-volume ratio. Additionally, there have been observations of pyrite with highly negative δ^{56}Fe values even after hydrothermal to low-grade metamorphic alteration. For example, Phanerozoic pyrite has been observed to retain negative δ^{56}Fe values up to temperatures of 300 °C (Dziony et al., 2014). Negative pyrite δ^{56}Fe values are also observed in Archean rocks that were exposed to hydrothermal alteration and/or metamorphic temperatures up to 550 °C (Yoshiya et al., 2015; Busigny et al., 2017). Minor alterations of pyrite δ^{56}Fe values cannot be ruled out but it is likely that if the initial δ^{56}Fe of a pyrite grain is negative, it cannot be modified to a positive δ^{56}Fe value unless it reacts with an Fe(II)-rich fluid during hydrothermal alteration or high-grade metamorphism. Therefore, pyrite δ^{56}Fe should be considered fairly robust to post-precipitation alteration over geological time scales and can therefore be used to infer environmental conditions during precipitation.

4.5.2. Interpretation of microscale pyrite δ^{56}Fe: active Fe redox cycling versus isotopic effects associated with pyrite precipitation in the absence of Fe(III)

Microscale isotopic analysis has revealed a ~ 8‰ variation in natural pyrite δ^{56}Fe, with values ranging from −4 to +4‰ (Nishizawa et al., 2010; Yoshiya et al., 2012; Agangi et al., 2015; Tahata et al., 2015; Galić et al., 2017; Sawaki et al., 2018). This isotopic range is also observed in Phanerozoic sediments deposited under oxygenated bottom waters (Virtasalo et al., 2013). These δ^{56}Fe variations have been interpreted to reflect active redox cycling of Fe. Specifically, positive pyrite δ^{56}Fe values are thought to reflect

Table 2
Compiled specific surface areas of pyrite as measured by the Brunauer-Emmett-Teller (BET) method.

Materials	Specific Surface Area (m^2/g)	References
Naturally-occurring (crushed)		
Sedimentary, 25-50 μm	0.43–0.59	Torrentó et al. (2010)
Sedimentary, 50–100 μm	0.62–0.88	Torrentó et al. (2010)
Unspecified origin, 38–45 μm	0.07	Moses and Herman (1991)
Unspecified origin, 63–250 μm	0.15	Gleisner et al. (2006)
Unspecified origin, 63–250 μm	0.17	Yan et al. (2018)
Unspecified origin, 125–250 μm	0.03	McKibben & Barnes (1986)
Unspecified origin, 150–250 μm	0.05	Williamson & Rimstidt (1994)
Unspecified origin, ball-milled	0.40	Vaclavkova et al. (2014)
Unspecified origin, micronized	1.90–2.40	Vaclavkova et al. (2014)
Naturally-occurring (separated)		
Lignite framboids, 1–5 μm	1.50–4.00	Pugh et al. (1981)
Sedimentary, 45–75 μm	0.21–5.37	Wolfe et al. (2016)
Hydrothermal, 45–75 μm	0.07–0.22	Wolfe et al. (2016)
Lignite massive pyrite, ≥50 μm	0.20–0.50	Pugh et al. (1981)
Experimentally synthesized		
~1 μm spherules	6.00	Harmandas et al. (1998)
Framboids, ~1 μm aggregates	2.90	Schippers & Jørgensen (2001)
Framboids, 5–10 nm crystals	1.03	Percak-Dennett et al. (2017)
Pyrite-marcasite mixture, 20–100 μm	0.41	Yan et al. (2018)

pyrite formed from Fe(III)-oxides derived from partial oxidation of a ferruginous water body or the residual portion remaining after dissimilatory iron reduction, while negative pyrite δ^{56}Fe values reflect pyrite formed from either residual $Fe(II)_{aq}$ (after Fe oxidation) or $Fe(II)_{aq}$ released from dissimilatory iron reduction of Fe(III)-oxides (Fig. 11). Negative δ^{56}Fe pyrite can be further divided into two types, with $\delta^{56}Fe \leq -3‰$ requiring both dissimilatory iron reduction and the KIE associated with precipitation, while δ^{56}Fe between 0 and −3‰ are consistent with either or both processes (Yoshiya et al., 2012).

Our study suggests that a similar range in microscale pyrite δ^{56}Fe can be explained solely by variations in pyrite precipitation rate from $Fe(II)_{aq}$, causing different relative expression of the KIE to the EIE at different stages in precipitation (Fig. 11). Specifically, we expect that incipient pyrite precipitation will be relatively fast compared to later-stage precipitation as Fe(II) and sulfide are consumed, perhaps as a function of depth of the water column or sedimentary column. We hypothesize that fast, incipient precipitation generates negative δ^{56}Fe values that dominate the grain population, while proportionally more positive δ^{56}Fe values are generated as precipitation rate decreases. In contrast, if pyrite precipitates in systems with extensive Fe redox cycling, we expect to see a more even distribution of positive δ^{56}Fe pyrite (from Fe(III)-oxides) and negative δ^{56}Fe pyrite (from $Fe(II)_{aq}$), although this also depends largely on the relative proportion of the sources. Analysis of pyrite δ^{56}Fe distributions at the individual grain scale may thus contribute to interpretation of microscale pyrite variation, whether it is caused by precipitation in environments with active Fe redox cycling or due to the intrinsic isotopic effects associated with pyrite precipitation from Fe(II) in the absence of Fe redox cycling.

4.5.3. Bulk pyrite δ^{56}Fe across the Great Oxidation Event (GOE)

At the bulk scale, a pronounced negative isotopic shift in pyrite δ^{56}Fe down to −3.5‰ has been observed in black shales between 2.3 and 2.8 Ga, which corresponds to the timing of the GOE (Rouxel et al., 2005). This negative shift has been interpreted to reflect changes in Fe cycling across the Archean-Proterozoic boundary, although the specific mechanism continues to be a subject of intense debate. The Archean ocean is thought to be Fe(II)-rich and oxygen-poor, with Fe primarily sourced from hydrothermal inputs with an estimated δ^{56}Fe of 0 to −0.5‰ (Yamaguchi et al., 2005). Rouxel et al. (2005) proposed that the negative δ^{56}Fe pyrite reflected an aqueous Fe(II) source that was distilled to negative values due to extensive oxidation of the Archean ocean. Severmann et al. (2008) proposed a "benthic Fe shuttle" mechanism, in which dissimilatory iron reduction on the continental shift provides isotopically light Fe(II) to the deep ocean from which pyrite formed. The extent of dissimilatory iron reduction was proposed to increase significantly at the end of the Archean due to the increase of Fe(III) substrate on an progressively oxygenated world (Johnson et al., 2008). Guilbaud et al. (2011b) alternatively proposed that the negative isotopic shift reflects the combined KIE associated with pyrite and FeS precipitation from an Fe(II)-rich ocean, but does not explain why the same negative shift is not observed throughout the Archean.

Based on our study, we propose a novel explanation for the negative pyrite δ^{56}Fe shift that is only observed at the Archean-Proterozoic boundary (Fig. 12). Despite the high level of $Fe(II)_{aq}$ in the Archean ocean, the rate of pyrite precipitation was likely low due to a lack of sulfide (derived from microbial reduction of sulfate, which is supposed to

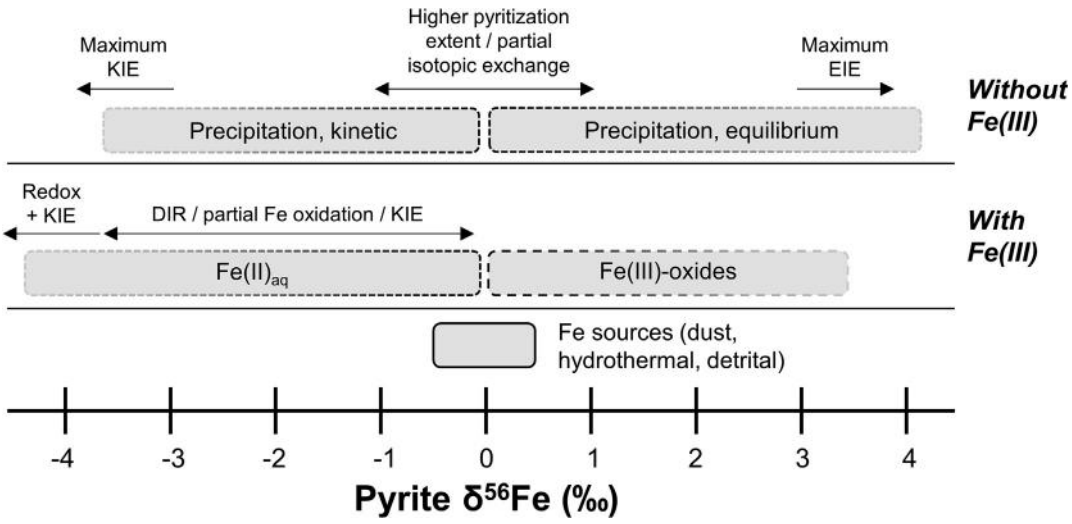

Fig. 11. Simplified diagram for the interpretation of microscale pyrite δ^{56}Fe variations in natural settings. Pyrite δ^{56}Fe may reflect the original Fe sources, which include dust, detrital, and hydrothermal sources with typical δ^{56}Fe range of −0.5 to +0.5‰ (e.g., Fantle and DePaolo, 2004; Yamaguchi et al., 2005; Kunzmann et al., 2017). In the presence of active Fe redox cycling, pyrite could be derived from negative δ^{56}Fe Fe(II)$_{aq}$ and positive δ^{56}Fe Fe(III). A combination of the kinetic isotopic effect (KIE) during precipitation with a source of low δ^{56}Fe Fe(II)$_{aq}$ (from partial Fe oxidation or dissimilatory iron reduction - DIR) can generate pyrite with δ^{56}Fe < −3.5‰. In the absence of Fe redox cycling, pyrite precipitated from Fe(II)$_{aq}$ can theoretically have δ^{56}Fe values that range from −3.5 to 4‰, with isotopic composition that is modulated by the pyritization extent and the relative expression of the KIE and EIE during precipitation.

have a low concentration – 2.5–200 μM – relative to the modern ocean – 28 mM; Habicht et al., 2002; Crowe et al., 2014) and oxidants that catalyze pyrite precipitation (e.g., S(0) or Mo(VI)$_{aq}$; this study; Schoonen and Barnes, 1991; Wilkin and Barnes, 1996). As oxygen slowly accumulated in the Archean atmosphere–ocean system, oxidative weathering supplied more sulfate and oxidants to the ocean, which drove sulfate reduction and consequent pyrite precipitation (e.g., Lyons et al., 2014; Robbins et al., 2016). The rate of pyrite precipitation during this time period

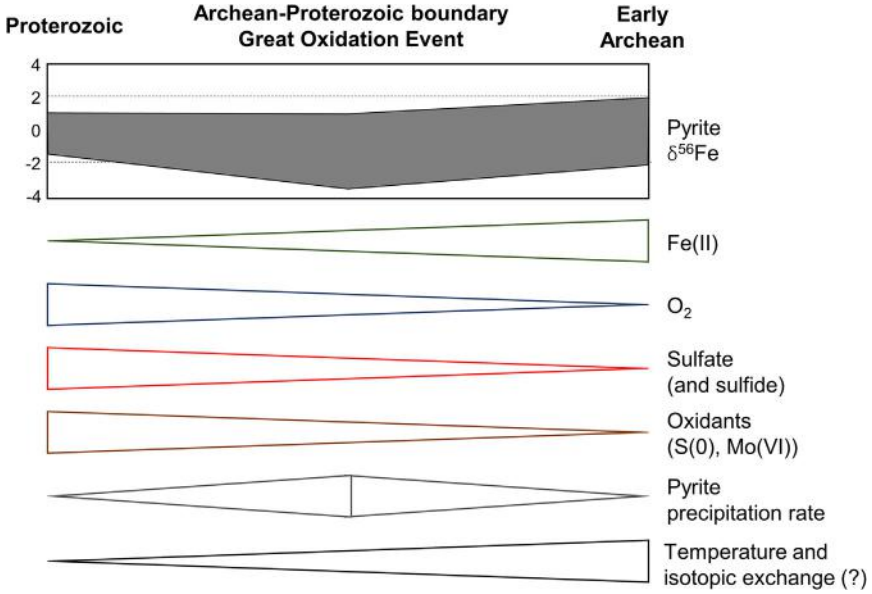

Fig. 12. Variations in pyrite δ^{56}Fe across the Great Oxidation Event along with the proposed simultaneous changes in chemical species availability and pyrite precipitation and isotopic exchange rate. The range of bulk pyrite δ^{56}Fe during the early Archean is constrained by averaging measurements of microscale pyrite δ^{56}Fe within various sampling sites (Nishizawa et al., 2010; Yoshiya et al., 2012, 2015; Marin-Carbonne et al., 2014; Galić et al., 2017). The early Archean ocean had low pyrite precipitation rates due to a lack of sulfide and oxidants. Oxygen accumulation in the late Archean led to higher sulfate and oxidant supplies into the Fe(II)-rich ocean, resulting in an increase in pyrite precipitation rate and the consequent formation of negative pyrite δ^{56}Fe values through larger expression of the kinetic isotope effect. After the Great Oxidation Event, pyrite precipitation rates are limited by the availability of Fe(II). Consequently, pyrite δ^{56}Fe shifts to higher values.

would have been higher compared to the early Archean due to a combination of the availability of Fe(II), sulfide, and oxidants such as S(0) and Mo(VI). During this time of incipient oxidation of the Earth surface, the Archean ocean may have undergone a gradual cooling on the order of 10–20 °C (Knauth, 2005; Robert and Chaussidon, 2006; Tartèse et al., 2017), which may have reduced the extent of isotopic exchange between pyrite and seawater Fe(II). Pyrite formed during this time would therefore have negative δ^{56}Fe values that reflected the KIE at high precipitation rates (i.e., low W values), which would have persisted until the Fe(II) ocean reservoir was depleted enough to distill isotopically. After the GOE, pyrite precipitation rates were likely limited by either the availability of sulfide and Fe (II) (in O_2-dominated systems) or Fe(II) (in sulfide-dominated systems). Distillation effects may explain why bulk pyrite δ^{56}Fe evolved to higher values (>0‰) just after the GOE. Thus, negative bulk pyrite δ^{56}Fe values did not arise except at the Archean-Proterozoic boundary. This hypothesis does not preclude the possibility of extensive oceanic Fe oxidation (Rouxel et al., 2005) or a benthic Fe shuttle (Severmann et al., 2008), but demonstrates that neither mechanism is required to explain the negative δ^{56}Fe shift. Our hypothesis also explains why the same negative δ^{56}Fe shift is not observed in the early Archean, which is the limitation for previous scenarios that are based primarily on sulfide and Fe(II) ratios in the ocean (Guilbaud et al., 2011b; Rolison et al., 2018).

5. SUMMARY

The sedimentary pyrite δ^{56}Fe record can be used to trace Fe biogeochemical cycling, microbial metabolism, and Earth's redox evolution over geological time scales, but the factors controlling the degree of isotopic fractionation associated with pyrite precipitation must be constrained. In this study, we have determined the apparent isotopic fractionation associated with pyrite precipitation at 80 °C to be -0.51 ± 0.22‰. This apparent isotopic fractionation is independent of the pathway (H_2S vs polysulfide) and the presence or absence of greigite. The observed isotopic fractionation is considerably smaller than the <−2‰ isotopic fractionations inferred from the Black Sea (Rolison et al., 2018) and constrained by experiments conducted at 40 °C and 100 °C (Guilbaud et al., 2011b). Modeling exercises suggest that isotopic exchange between pyrite and $Fe(II)_{aq}$ occurs over experimental time scales and shifts pyrite δ^{56}Fe towards more positive values as the EIE is expressed to a greater degree. Pyrite δ^{56}Fe values may also be affected by a rate-dependent KIE or a difference in the isotopic fractionation factor associated with nucleation compared to growth.

Through modeling approaches, we infer that isotopic exchange rates decrease with time, most likely as a result of increasing particle size. The current (admittedly limited) experimental data suggest that the isotopic exchange rate is not necessarily correlated with temperature, and the best estimate for the isotopic exchange rate constant (k_{pyrite_ex}) between pyrite and $Fe(II)_{aq}$ at low temperatures ranges from 10^{-19} to 10^{-11} mol/L/s. Over this large range, sedimentary pyrite precipitation may theoretically express the full spectrum of the KIE and the EIE with a δ^{56}Fe range of −3 to >4‰. The existence of predominantly negative pyrite δ^{56}Fe values in modern settings suggests that the KIE is preferentially expressed in sedimentary settings but does not rule out expression of the EIE in modern environments. For isotopic exchange to be completely irrelevant to pyrite precipitation in low temperature settings, k_{pyrite_ex} must be $<10^{-16}$ mol/L/s. Experiments that can constrain the isotopic exchange rate between pyrite and $Fe(II)_{aq}$ at low temperatures are required. It is important to emphasize that all studies performed to date have been performed under abiotic conditions. Microbial life (especially sulfate-reducing bacteria) is pervasive throughout pyrite-forming environments and future studies that focus on constraining microbial effects on the Fe isotopic fractionation associated with pyrite precipitation are urgently needed.

Our study has implications for the interpretation of pyrite-based Fe isotope records. Multiple lines of evidence suggest that ancient pyrite retains its primary isotopic composition and is not altered during post-formational exchange with $Fe(II)_{aq}$. At the micro-scale, pyrite δ^{56}Fe variation can be interpreted to reflect the relative expression of the KIE and EIE associated with different stages of pyrite precipitation from $Fe(II)_{aq}$ rather than reflecting active redox cycling of Fe between Fe(II) and Fe(III). Similarly, the negative shift of bulk pyrite δ^{56}Fe near the GOE may reflect increases in precipitation rate (relative to isotopic exchange) due to the combined availability of Fe(II), sulfate/sulfide, and oxidants, which arise specifically during this period of incipient oxidation in Earth's history. Ultimately, our study provides a novel framework for interpreting the pyrite-based Fe isotope records.

ACKNOWLEDGEMENTS

This work was supported by the National Aeronautics and Space Administration (grant code NASA-NAI-NNA09DA76A) awarded via Penn State Astrobiology Center to co-PI MSF. MM acknowledges support from the Hiroshi & Koya Ohmoto Graduate Fellowship through the Geosciences department of Penn State University. We thank Jennifer Macalady for providing guidance and Huimin Yu, Scott Hynek, and Matthew Gonzales for help in setting up the Fe isotopic and concentration analyses. We also thank the associate editor (Jeffrey Alt) and the reviewers (Vincent Busigny, Romain Guilbaud, and Clark Johnson) for their constructive comments that helped to improve the manuscript.

APPENDIX A. SUPPLEMENTARY MATERIAL

Supplementary data to this article can be found online at https://doi.org/10.1016/j.gca.2019.03.017.

REFERENCES

Agangi A., Hofmann A., Rollion-Bard C., Marin-Carbonne J., Cavalazzi B., Large R. and Meffre S. (2015) Gold accumulation in the Archaean Witwatersrand Basin, South Africa—Evidence from concentrically laminated pyrite. *Earth-Sci. Rev.* **140**, 27–53.

Archer C. and Vance D. (2006) Coupled Fe and S isotope evidence for Archean microbial Fe(III) and sulfate reduction. *Geology* **34**, 153–156.

Balci N., Bullen T. D., Witte-Lien K., Shanks W. C., Motelica M. and Mandernack K. W. (2006) Iron isotope fractionation during microbially stimulated Fe(II) oxidation and Fe(III) precipitation. *Geochim. Cosmochim. Acta* **70**, 622–639.

Beard B. L., Handler R. M., Scherer M. M., Wu L., Czaja A. D., Heimann A. and Johnson C. M. (2010) Iron isotope fractionation between aqueous ferrous iron and goethite. *Earth Planet. Sci. Lett.* **295**, 241–250.

Beard B. L., Johnson C. M., Von Damm K. L. and Poulson R. L. (2003) Iron isotope constraints on Fe cycling and mass balance in oxygenated Earth oceans. *Geology* **31**, 629–632.

Benning L. G., Wilkin R. T. and Barnes H. L. (2000) Reaction pathways in the Fe-S system below 100°C. *Chem. Geol.* **167**, 25–51.

Berner R. A. (1984) Sedimentary pyrite formation: an update. *Geochim. Cosmochim. Acta* **48**, 605–615.

Blanchard M., Poitrasson F., Méheut M., Lazzeri M., Mauri F. and Balan E. (2009) Iron isotope fractionation between pyrite (FeS_2), hematite (Fe_2O_3) and siderite ($FeCO_3$): A first-principles density functional theory study. *Geochim. Cosmochim. Acta* **73**, 6565–6578.

Boursiquot S., Mullet M., Abdelmoula M., Génin J.-M. and Ehrhardt J.-J. (2001) The dry oxidation of tetragonal FeS_{1-x} mackinawite. *Phys. Chem. Miner.* **28**, 600–611.

Brantley S. L., Liermann L. and Bullen T. (2001) Fractionation of Fe isotopes by soil microbes and organic acids. *Geology* **29**, 535–538.

Brantley S. L., Liermann L. J., Guynn R. L., Anbar A., Icopini G. A. and Barling J. (2004) Fe isotopic fractionation during mineral dissolution with and without bacteria. *Geochim. Cosmochim. Acta* **68**, 3189–3204.

Busigny V., Marin-Carbonne J., Muller E., Cartigny P., Rollion-Bard C., Assayag N. and Philippot P. (2017) Iron and sulfur isotope constraints on redox conditions associated with the 3.2 Ga barite deposits of the Mapepe Formation (Barberton Greenstone Belt, South Africa). *Geochim. Cosmochim. Acta* **210**, 247–266.

Busigny V., Planavsky N. J., Jézéquel D., Crowe S., Louvat P., Moureau J., Viollier E. and Lyons T. W. (2014) Iron isotopes in an Archean ocean analogue. *Geochim. Cosmochim. Acta* **133**, 443–462.

Butler I. B., Archer C., Vance D., Oldroyd A. and Rickard D. (2005) Fe isotope fractionation on FeS formation in ambient aqueous solution. *Earth Planet. Sci. Lett.* **236**, 430–442.

Butler I. B. and Rickard D. (2000) Framboidal pyrite formation via the oxidation of iron (II) monosulfide by hydrogen sulphide. *Geochim. Cosmochim. Acta* **64**, 2665–2672.

Canfield D. E. (1989) Reactive iron in marine sediments. *Geochim. Cosmochim. Acta* **53**, 619–632.

Canfield D. E. (2005) The early history of atmospheric oxygen: Homage to Robert M. Garrels. *Annu. Rev. Earth Planet. Sci.* **33**, 1–36.

Canfield D. E., Thamdrup B. and Fleischer S. (1998) Isotope fractionation and sulfur metabolism by pure and enrichment cultures of elemental sulfur-disproportionating bacteria. *Limnol. Oceanogr.* **43**, 253–264.

Chever F., Rouxel O. J., Croot P. L., Ponzevera E., Wuttig K. and Auro M. (2015) Total dissolvable and dissolved iron isotopes in the water column of the Peru upwelling regime. *Geochim. Cosmochim. Acta* **162**, 66–82.

Croal L. R., Johnson C. M., Beard B. L. and Newman D. K. (2004) Iron isotope fractionation by Fe(II)-oxidizing photoautotrophic bacteria. *Geochim. Cosmochim. Acta* **68**, 1227–1242.

Crosby H. A., Roden E. E., Johnson C. M. and Beard B. L. (2007) The mechanisms of iron isotope fractionation produced during dissimilatory Fe(III) reduction by *Shewanella putrefaciens* and *Geobacter sulfurreducens*. *Geobiology* **5**, 169–189.

Crowe S. A., Paris G., Katsev S., Jones C., Kim S.-T., Zerkle A. L., Nomosatryo S., Fowle D. A., Adkins J. F., Sessions A. L., Farquhar J. and Canfield D. E. (2014) Sulfate was a trace constituent of Archean seawater. *Science (80-)* **346**, 735–739.

Czaja A. D., Johnson C. M., Beard B. L., Eigenbrode J. L., Freeman K. H. and Yamaguchi K. E. (2010) Iron and carbon isotope evidence for ecosystem and environmental diversity in the ~2.7 to 2.5 Ga Hamersley Province, Western Australia. *Earth Planet. Sci. Lett.* **292**, 170–180.

Czaja A. D., Johnson C. M., Roden E. E., Beard B. L., Voegelin A. R., Nägler T. F., Beukes N. J. and Wille M. (2012) Evidence for free oxygen in the Neoarchean ocean based on coupled iron-molybdenum isotope fractionation. *Geochim. Cosmochim. Acta* **86**, 118–137.

d'Abzac F. X., Czaja A. D., Beard B. L., Schauer J. J. and Johnson C. M. (2014) Iron distribution in size-resolved aerosols generated by UV-femtosecond laser ablation: Influence of cell geometry and implications for in situ isotopic determination by LA-MC-ICP-MS. *Geostand. Geoanalytical Res.* **38**, 293–309.

DePaolo D. J. (2011) Surface kinetic model for isotopic and trace element fractionation during precipitation of calcite from aqueous solutions. *Geochim. Cosmochim. Acta* **75**, 1039–1056.

Dideriksen K., Baker J. A. and Stipp S. L. S. (2008) Equilibrium Fe isotope fractionation between inorganic aqueous Fe(III) and the siderophore complex, Fe(III)-desferrioxamine B. *Earth Planet. Sci. Lett.* **269**, 280–290.

Domagal-Goldman S. D. and Kubicki J. D. (2008) Density functional theory predictions of equilibrium isotope fractionation of iron due to redox changes and organic complexation. *Geochim. Cosmochim. Acta* **72**, 5201–5216.

Dziony W., Horn I., Lattard D., Koepke J., Steinhoefel G., Schuessler J. A. and Holtz F. (2014) In-situ Fe isotope ratio determination in Fe-Ti oxides and sulfides from drilled gabbros and basalt from the IODP Hole 1256D in the eastern equatorial Pacific. *Chem. Geol.* **363**, 101–113.

Fantle M. S., Maher K. M. and DePaolo D. J. (2010) Isotopic Approaches for Quantifying the Rates of Marine Burial Diagenesis. *Reviews of Geophysics* **48**(RG3002), 30. https://doi.org/10.1029/2009RG000306.

Fantle M. S. and DePaolo D. J. (2007) Ca isotopes in carbonate sediment and pore fluid from ODP Site 807A: The Ca^{2+}(aq)-calcite equilibrium fractionation factor and calcite recrystallization rates in Pleistocene sediments. *Geochim. Cosmochim. Acta* **71**, 2524–2546.

Fantle M. S. and DePaolo D. J. (2004) Iron isotopic fractionation during continental weathering. *Earth Planet. Sci. Lett.* **228**, 547–562.

Fehr M. A., Andersson P. S., Hålenius U., Gustafsson O. and Morth C. M. (2010) Iron enrichments and Fe isotopic compositions of surface sediments from the Gotland Deep, Baltic Sea. *Chem. Geol.* **277**, 310–322.

Fossing H. (1990) Sulfate reduction in shelf sediments in the upwelling region off Central peru. *Cont. Shelf Res.* **10**, 355–367.

Fossing H., Thode-Andersen S. and Jørgensen B. B. (1992) Sulfur isotope exchange between ^{35}S-labeled inorganic sulfur compounds in anoxic marine sediments. *Mar. Chem.* **38**, 117–132.

Fujii T., Moynier F., Blichert-Toft J. and Albarède F. (2014) Density functional theory estimation of isotope fractionation of Fe, Ni, Cu, and Zn among species relevant to geochemical and biological environments. *Geochim. Cosmochim. Acta* **140**, 553–576.

Galić A., Mason P. R. D., Mogollón J. M., Wolthers M., Vroon P. Z. and Whitehouse M. J. (2017) Pyrite in a sulfate-poor Paleoarchean basin was derived predominantly from elemental sulfur: Evidence from 3.2 Ga sediments in the Barberton Greenstone Belt, Kaapvaal Craton. *Chem. Geol.* **449**, 135–146.

Gleisner M., Herbert R. B. and Kockum Frogner P. C. (2006) Pyrite oxidation by *Acidithiobacillus ferrooxidans* at various concentrations of dissolved oxygen. *Chem. Geol.* **225**, 16–29.

Gorski C. A. and Fantle M. S. (2017) Stable mineral recrystallization in low temperature aqueous systems: a critical review. *Geochim. Cosmochim. Acta* **198**, 439–465.

Graham S., Pearson N., Jackson S., Griffin W. and O'Reilly S. Y. (2004) Tracing Cu and Fe from source to porphyry: In situ determination of Cu and Fe isotope ratios in sulfides from the Grasberg Cu-Au deposit. *Chem. Geol.* **207**, 147–169.

Guelke M. and Von Blanckenburg F. (2007) Fractionation of stable iron isotopes in higher plants. *Environ. Sci. Technol.* **41**, 1896–1901.

Guilbaud R., Butler I. B. and Ellam R. M. (2011b) Abiotic pyrite formation produces a large Fe isotope fractionation. *Science (80-)* **332**, 1548–1551.

Guilbaud R., Butler I. B., Ellam R. M. and Rickard D. (2010) Fe isotope exchange between $Fe(II)_{aq}$ and nanoparticulate mackinawite (FeS_m) during nanoparticle growth. *Earth Planet. Sci. Lett.* **300**, 174–183.

Guilbaud R., Butler I. B., Ellam R. M., Rickard D. and Oldroyd A. (2011a) Experimental determination of the equilibrium Fe isotope fractionation between Fe^{2+}_{aq} and FeS_m (mackinawite) at 25 and 2°C. *Geochim. Cosmochim. Acta* **75**, 2721–2734.

Habicht K. S., Gade M., Thamdrup B., Berg P. and Canfield D. E. (2002) Calibration of sulfate levels in the Archean ocean. *Science (80-)* **298**, 2372–2374.

Harmandas N. G., Navarro Fernandez E. and Koutsoukos P. G. (1998) Crystal growth of pyrite in aqueous solutions. Inhibition by organophosphorus compounds. *Langmuir* **14**, 1250–1255.

Howarth R. W. and Jorgensen B. B. (1984) Formation of ^{35}S-labeled elemental sulfur and pyrite in coastal marine sediment (Limfjorden and Kysing Fjord, Denmark) during short-term 35SO42- reduction measurments. *Geochim. Cosmochim. Acta* **48**, 1807–1818.

Huerta-Diaz M. A. and Morse J. W. (1990) A quantitative method for determination of trace metal concentrations in sedimentary pyrite. *Mar. Chem.* **29**, 119–144.

Icopini G. A., Anbar A. D., Ruebush S. S., Tien M. and Brantley S. L. (2004) Iron isotope fractionation during microbial reduction of iron: the importance of adsorption. *Geology* **32**, 205–208.

Johnson C. M., Beard B. L. and Roden E. E. (2008) The iron isotope fingerprints of redox and biogeochemical cycling in modern and ancient Earth. *Annu. Rev. Earth Planet. Sci.* **36**, 457–493.

Johnson C. M., Roden E. E., Welch S. A. and Beard B. L. (2005) Experimental constraints on Fe isotope fractionation during magnetite and Fe carbonate formation coupled to dissimilatory hydrous ferric oxide reduction. *Geochim. Cosmochim. Acta* **69**, 963–993.

Johnson C. M., Skulan J. L., Beard B. L., Sun H., Nealson K. H. and Braterman P. S. (2002) Isotopic fractionation between Fe (III) and Fe(II) in aqueous solutions. *Earth Planet. Sci. Lett.* **195**, 141–153.

Johnston D. T., Wolfe-Simon F., Pearson A. and Knoll A. H. (2009) Anoxygenic photosynthesis modulated Proterozoic oxygen and sustained Earth's middle age. *Proc. Natl. Acad. Sci. U. S. A.* **106**, 16925–16929.

Kamyshny A., Goifman A., Gun J., Rizkov D. and Lev O. (2004) Equilibrium distribution of polysulfide ions in aqueous solutions at 25 degrees C: a new approach for the study of polysulfides' equilibria. *Environ. Sci. Technol.* **38**, 6633–6644.

Kappler A., Johnson C. M., Crosby H. A., Beard B. L. and Newman D. K. (2010) Evidence for equilibrium iron isotope fractionation by nitrate-reducing iron (II)-oxidizing bacteria. *Geochim. Cosmochim. Acta* **74**, 2826–2842.

Kiczka M., Wiederhold J. G., Kraemer S. M., Bourdon B. and Kretzschmar R. (2010) Iron isotope fractionation during Fe uptake and translocation in alpine plants. *Environ. Sci. Technol.* **44**, 6144–6150.

Knauth L. P. (2005) Temperature and salinity history of the Precambrian ocean: Implications for the course of microbial evolution. *Palaeogeogr. Palaeoclimatol. Palaeoecol.* **219**, 53–69.

Kunzmann M., Gibson T. M., Halverson G. P., Hodgskiss M. S. W., Bui T. H., Carozza D. A., Sperling E. A., Poirier A., Cox G. M. and Wing B. A. (2017) Iron isotope biogeochemistry of Neoproterozoic marine shales. *Geochim. Cosmochim. Acta* **209**, 85–105.

Lan Y. and Butler E. C. (2014) Monitoring the transformation of mackinawite to greigite and pyrite on polymer supports. *Appl. Geochem.* **50**, 1–6.

Lein A. Y. (1983) Biogeochemistry of the anaerobic diagenesis of recent Baltic Sea sediments. *Ecol. Bull.* **35**, 441–461.

Lennie A. R. (1995) Synthesis and Rietveld crystal structure refinement of mackinawite, tetragonal FeS. *Mineral. Mag.* **59**, 677–683.

Liermann L. J., Mathur R., Wasylenki L. E., Nuester J., Anbar A. D. and Brantley S. L. (2011) Extent and isotopic composition of Fe and Mo release from two Pennsylvania shales in the presence of organic ligands and bacteria. *Chem. Geol.* **281**, 167–180.

Lin S., Huang K.-M. and Chen S.-K. (2000) Organic carbon deposition and its control on iron sulfide formation of the southern East China Sea continental shelf sediments. *Cont. Shelf Res.* **20**, 619–635.

Lin S., Huang K. and Chen S. (2002) Sulfate reduction and iron sulfide mineral formation in the southern East China Sea continental slope sediment. *Deep Sea Res. Part I Oceanogr. Res. Pap.* **49**, 1837–1852.

Lin S. and Morse J. (1991) Sulfate reduction and iron sulfide mineral formation in Gulf of Mexico anoxic sediments. *Am. J. Sci.* **291**, 55–89.

Lin Z., Sun X., Lu Y., Strauss H., Xu L., Gong J., Teichert B. M. A., Lu R., Lu H., Sun W. and Peckmann J. (2017) The enrichment of heavy iron isotopes in authigenic pyrite as a possible indicator of sulfate-driven anaerobic oxidation of methane: Insights from the South China Sea. *Chem. Geol.* **449**, 15–29.

Liu K., Wu L., Couture R.-M., Li W. and Van Cappellen P. (2015) Iron isotope fractionation in sediments of an oligotrophic freshwater lake. *Earth Planet. Sci. Lett.* **423**, 164–172.

Luther G. W. (1991) Pyrite synthesis via polysulfide compounds. *Geochim. Cosmochim. Acta* **55**, 2839–2849.

Lyons T. W., Reinhard C. T. and Planavsky N. J. (2014) The rise of oxygen in Earth's early ocean and atmosphere. *Nature* **506**, 307–315.

Maher K., DePaolo D. J. and Lin J. C. F. (2004) Rates of silicate dissolution in deep-sea sediment: In situ measurement using $^{234}U/^{238}U$ of pore fluids. *Geochim. Cosmochim. Acta* **68**, 4629–4648.

Maher K., Steefel C. I., DePaolo D. J. and Viani B. E. (2006) The mineral dissolution rate conundrum: Insights from reactive transport modeling of U isotopes and pore fluid chemistry in marine sediments. *Geochim. Cosmochim. Acta* **70**, 337–363.

Marin-Carbonne J., Rollion-Bard C., Bekker A., Rouxel O., Agangi A., Cavalazzi B., Wohlgemuth-Ueberwasser C. C., Hofmann A. and McKeegan K. D. (2014) Coupled Fe and S isotope variations in pyrite nodules from Archean shale. *Earth Planet. Sci. Lett.* **392**, 67–79.

McKibben M. A. and Barnes H. L. (1986) Oxidation of pyrite in low temperature acidic solutions: rate laws and surface textures. *Geochim. Cosmochim. Acta* **50**, 1509–1520.

Morin G., Noël V., Menguy N., Brest J., Baptiste B., Tharaud M., Ona-Nguema G., Ikogou M., Viollier E. and Juillot F. (2017) Nickel accelerates pyrite nucleation at ambient temperature. *Geochem. Perspect. Lett.*, 6–11.

Morse J. W., Arvidson R. S. and Lüttge A. (2007) Calcium carbonate formation and dissolution. *Chem. Rev.* **107**, 342–381.

Morse J. W. and Wang Q. (1997) Pyrite formation under conditions approximating those in anoxic sediments: II. Influence of precursor iron minerals and organic matter. *Mar. Chem.* **57**, 187–193.

Moses C. O. and Herman J. S. (1991) Pyrite oxidation at circumneutral pH. *Geochim. Cosmochim. Acta* **55**, 471–482.

Mulholland D. S., Poitrasson F., Shirokova L. S., González A. G., Pokrovsky O. S., Boaventura G. R. and Vieira L. C. (2015) Iron isotope fractionation during Fe(II) and Fe(III) adsorption on cyanobacteria. *Chem. Geol.* **400**, 24–33.

Nishizawa M., Yamamoto H., Ueno Y., Tsuruoka S., Shibuya T., Sawaki Y., Yamamoto S., Kon Y., Kitajima K., Komiya T., Maruyama S. and Hirata T. (2010) Grain-scale iron isotopic distribution of pyrite from Precambrian shallow marine carbonate revealed by a femtosecond laser ablation multicollector ICP-MS technique: possible proxy for the redox state of ancient seawater. *Geochim. Cosmochim. Acta* **74**, 2760–2778.

Ohmoto H., Watanabe Y., Lasaga A. C., Naraoka H., Johnson I., Brainard J. and Chorney A. (2014) Oxygen, iron, and sulfur geochemical cycles on early Earth: Paradigms and contradictions. *Geol. Soc. Am. Spec. Pap.* **504**, 55–95.

Pankow J. and Morgan J. (1979) Dissolution of tetragonal ferrous sulfide (mackinawite) in anoxic aqueous systems. 1. Dissolution rate as a function of pH, temperature, and ionic strength. *Environ. Sci. Technol.* **13**, 1248–1255.

Peiffer S., Behrends T., Hellige K., Larese-Casanova P., Wan M. and Pollok K. (2015) Pyrite formation and mineral transformation pathways upon sulfidation of ferric hydroxides depend on mineral type and sulfide concentration. *Chem. Geol.* **400**, 44–55.

Percak-Dennett E., He S., Converse B., Konishi H., Xu H., Corcoran A., Noguera D., Chan C., Bhattacharyya A., Borch T., Boyd E. and Roden E. E. (2017) Microbial acceleration of aerobic pyrite oxidation at circumneutral pH. *Geobiology* **15**, 690–703.

Percak-Dennett E. M., Beard B. L., Xu H., Konishi H., Johnson C. M. and Roden E. E. (2011) Iron isotope fractionation during microbial dissimilatory iron oxide reduction in simulated Archaean seawater. *Geobiology* **9**, 205–220.

Percak-Dennett E. M., Loizeau J. L., Beard B. L., Johnson C. M. and Roden E. E. (2013) Iron isotope geochemistry of biogenic magnetite-bearing sediments from the Bay of Vidy, Lake Geneva. *Chem. Geol.* **360–361**, 32–40.

Polyakov V. B. and Soultanov D. M. (2011) New data on equilibrium iron isotope fractionation among sulfides: Constraints on mechanisms of sulfide formation in hydrothermal and igneous systems. *Geochim. Cosmochim. Acta* **75**, 1957–1974.

Pugh C., Hossner L. and Dixon J. (1981) Pyrite and marcasite surface area as influenced by morphology and particle diameter. *Soil Sci. Soc. Am. J.* **45**, 979–982.

Reeves D. and Rothman D. H. (2013) Age dependence of mineral dissolution and precipitation rates. *Glob. Biogeochem. Cycl.* **27**, 906–919.

Rickard D. (1975) Kinetics and mechanism of pyrite formation at low temperatures. *Am. J. Sci.* **275**, 636–652.

Rickard D. (1997) Kinetics of pyrite formation by the H_2S oxidation of iron (II) monosulfide in aqueous solutions between 25 and 125°C: The rate equation. *Geochim. Cosmochim. Acta* **61**, 115–134.

Rickard D. (2006) The solubility of FeS. *Geochim. Cosmochim. Acta* **70**, 5779–5789.

Rickard D., Butler I. B. and Oldroyd A. (2001) A novel iron sulphide mineral switch and its implications for earth and planetary science. *Earth Planet. Sci. Lett.* **189**, 85–91.

Rickard D., Grimes S., Butler I., Oldroyd A. and Davies K. L. (2007) Botanical constraints on pyrite formation. *Chem. Geol.* **236**, 228–246.

Rickard D. and Luther G. W. (2007) Chemistry of iron sulfides. *Chem. Rev.* **107**, 514–562.

Rickard D. and Morse J. W. (2005) Acid volatile sulfide (AVS). *Mar. Chem.* **97**, 141–197.

Robbins L. J., Lalonde S. V., Planavsky N. J., Partin C. A., Reinhard C. T., Kendall B., Scott C., Hardisty D. S., Gill B. C., Alessi D. S., Dupont C. L., Saito M. A., Crowe S. A., Poulton S. W., Bekker A., Lyons T. W. and Konhauser K. O. (2016) Trace elements at the intersection of marine biological and geochemical evolution. *Earth-Science Rev.* **163**, 323–348.

Robert F. and Chaussidon M. (2006) A palaeotemperature curve for the Precambrian oceans based on silicon isotopes in cherts. *Nature* **443**, 969–972.

Rodushkin I., Stenberg A., Andren H., Malinovsky D. and Baxter D. C. (2004) Isotopic fractionation during diffusion of transition metal ions in solution. *Anal. Chem.* **76**, 2148–2151.

Roerdink D. L., van den Boorn S. H. J. M., Geilert S., Vroon P. Z. and van Bergen M. J. (2015) Experimental constraints on kinetic and equilibrium silicon isotope fractionation during the formation of non-biogenic chert deposits. *Chem. Geol.* **402**, 40–51.

Rolison J. M., Stirling C. H., Middag R., Gault-Ringold M., George E. and Rijkenberg M. J. A. (2018) Iron isotope fractionation during pyrite formation in a sulfidic Precambrian ocean analogue. *Earth Planet. Sci. Lett.* **488**, 1–13.

Rouxel O., Fouquet Y. and Ludden J. N. (2004) Subsurface processes at the Lucky Strike hydrothermal field, Mid-Atlantic Ridge: Evidence from sulfur, selenium, and iron isotopes. *Geochim. Cosmochim. Acta* **68**, 2295–2311.

Rouxel O. J. and Auro M. (2010) Iron isotope variations in coastal seawater determined by multicollector ICP-MS. *Geostand. Geoanal. Res.* **34**, 135–144.

Rouxel O. J., Bekker A. and Edwards K. J. (2005) Iron isotope constraints on the Archean and Paleproterozoic ocean redox state. *Science (80-)* **307**, 1088–1091.

Rouxel O., Shanks W. C., Bach W. and Edwards K. J. (2008) Integrated Fe- and S-isotope study of seafloor hydrothermal vents at East Pacific Rise 9–10°N. *Chem. Geol.* **252**, 214–227.

Rustad J. R., Casey W. H., Yin Q. Z., Bylaska E. J., Felmy A. R., Bogatko S. A., Jackson V. E. and Dixon D. A. (2010) Isotopic fractionation of Mg^{2+}(aq), Ca^{2+}(aq), and Fe^{2+}(aq) with carbonate minerals. *Geochim. Cosmochim. Acta* **74**, 6301–6323.

Sand K. K., Tobler D. J., Dobberschütz S., Larsen K. K., Makovicky E., Andersson M. P., Wolthers M. and Stipp S. L. S. (2016) Calcite growth kinetics: dependence on saturation index, Ca^{2+}:CO_3^{2-} activity ratio, and surface atomic structure. *Cryst. Growth Des.* **16**, 3602–3612.

Sawaki Y., Tahata M., Komiya T., Hirata T., Han J. and Shu D. (2018) Redox history of the Three Gorges region during the Ediacaran and Early Cambrian as indicated by the Fe isotope. *Geosci. Front.* **9**, 155–172.

Schippers A. and Jørgensen B. B. (2001) Oxidation of pyrite and iron sulfide by manganese dioxide in marine sediments. *Geochim. Cosmochim. Acta* **65**, 915–922.

Scholz F., Severmann S., McManus J., Noffke A., Lomnitz U. and Hensen C. (2014) On the isotope composition of reactive iron in

marine sediments: Redox shuttle versus early diagenesis. *Chem. Geol.* **389**, 48–59.

Schoonen M. A. (2004) Mechanisms of sedimentary pyrite formation. *Geol. Soc. Am. Spec. Pap.* **379**(379), 117–134.

Schoonen M. A. and Barnes H. L. (1991) Reactions forming pyrite and marcasite from solution: II. Via FeS precursors below 100° C. *Geochim. Cosmochim. Acta* **55**, 1505–1514.

Severmann S., Johnson C. M., Beard B. L. and McManus J. (2006) The effect of early diagenesis on the Fe isotope compositions of porewaters and authigenic minerals in continental margin sediments. *Geochim. Cosmochim. Acta* **70**, 2006–2022.

Severmann S., Lyons T. W., Anbar A., McManus J. and Gordon G. (2008) Modern iron isotope perspective on the benthic iron shuttle and the redox evolution of ancient oceans. *Geology* **36**, 487–490.

Shi B., Liu K., Wu L., Li W., Smeaton C. M., Beard B. L., Johnson C. M., Roden E. E. and Van Cappellen P. (2016) Iron isotope fractionations reveal a finite bioavailable Fe pool for structural Fe(III) reduction in nontronite. *Environ. Sci. Technol.*.

Skulan J., Beard B. and Johnson C. (2002) Kinetic and equilibrium Fe isotope fractionation between aqueous Fe (III) and hematite. *Geochim. Cosmochim. Acta* **66**, 2995–3015.

Steefel C. I., Appelo C. A. J., Arora B., Jacques D., Kalbacher T., Kolditz O., Lagneau V., Lichtner P. C., Mayer K. U., Meussen J. C. L., Molins S., Moulton D., Shao H., Šimůnek J., Spycher N., Yabusaki S. B. and Yeh G. T. (2015) Reactive transport codes for subsurface environmental simulation. *Comput. Geosci.* **19**, 445–478.

Sweeney R. E. and Kaplan I. R. (1973) Pyrite framboid formation: Laboratory synthesis and marine sediments. *Econ. Geol.* **68**, 618–634.

Syverson D. D., Borrok D. M. and Seyfried W. E. (2013) Experimental determination of equilibrium Fe isotopic fractionation between pyrite and dissolved Fe under hydrothermal conditions. *Geochim. Cosmochim. Acta* **122**, 170–183.

Tahata M., Sawaki Y., Yoshiya K., Nishizawa M., Komiya T., Hirata T., Yoshida N., Maruyama S. and Windley B. F. (2015) The marine environments encompassing the Neoproterozoic glaciations: evidence from C, Sr and Fe isotope ratios in the Hecla Hoek Supergroup in Svalbard. *Precambrian Res.* **263**, 19–42.

Tang J., Dietzel M., Böhm F., Köhler S. J. and Eisenhauer A. (2008) Sr^{2+}/Ca^{2+} and $^{44}Ca/^{40}Ca$ fractionation during inorganic calcite formation: II. Ca isotopes. *Geochim. Cosmochim. Acta* **72**, 3733–3745.

Tangalos G. E., Beard B. L., Johnson C. M., Alpers C. N., Shelobolina E. S., Xu H., Konishi H. and Roden E. E. (2010) Microbial production of isotopically light iron(II) in a modern chemically precipitated sediment and implications for isotopic variations in ancient rocks. *Geobiology* **8**, 197–208.

Tartèse R., Chaussidon M., Gurenko A., Delarue F. and Robert F. (2017) Warm Archaean oceans reconstructed from oxygen isotope composition of early-life remnants. *Geochem. Perspect. Lett.*, 55–65.

Teutsch N., von Gunten U., Porcelli D., Cirpka O. A. and Halliday A. N. (2005) Adsorption as a cause for iron isotope fractionation in reduced groundwater. *Geochim. Cosmochim. Acta* **69**, 4175–4185.

Teutsch N., Schmid M., Müller B., Halliday A. N., Bürgmann H. and Wehrli B. (2009) Large iron isotope fractionation at the oxic-anoxic boundary in Lake Nyos. *Earth Planet. Sci. Lett.* **285**, 52–60.

Thode-Andersen S. and Jørgensen B. B. (1989) Sulfate reduction and the formation of ^{35}S-labeled FeS, FeS_2, and S^o in coastal marine sediments. *Limnol. Oceanogr.* **34**, 793–806.

Toner B. M., Rouxel O. J., Santelli C. M., Bach W. and Edwards K. J. (2016) Iron transformation pathways and redox microenvironments in seafloor sulfide-mineral deposits: Spatially resolved Fe XAS and $\delta^{57/54}$Fe observations. *Front. Microbiol.* **7**, 1–17.

Torrentó C., Cama J., Urmeneta J., Otero N. and Soler A. (2010) Denitrification of groundwater with pyrite and *Thiobacillus denitrificans*. *Chem. Geol.* **278**, 80–91.

Vaclavkova S., Jørgensen C. J., Jacobsen O. S., Aamand J. and Elberling B. (2014) The importance of microbial iron sulfide oxidation for nitrate depletion in anoxic Danish sediments. *Aquat. Geochem.* **20**, 419–435.

Virtasalo J. J., Whitehouse M. J. and Kotilainen A. T. (2013) Iron isotope heterogeneity in pyrite fillings of Holocene worm burrows. *Geology* **41**, 39–42.

Wan M., Schröder C. and Peiffer S. (2017) Fe(III):S(-II) concentration ratio controls the pathway and the kinetics of pyrite formation during sulfidation of ferric hydroxides. *Geochim. Cosmochim Acta*.

Wang Q. and Morse J. W. (1996) Pyrite formation under conditions approximating those in anoxic sediments I. Pathway and morphology. *Mar. Chem.* **52**, 99–121.

Wasylenki L. E., Anbar A. D., Liermann L. J., Mathur R., Gordon G. W. and Brantley S. L. (2007) Isotope fractionation during microbial metal uptake measured by MC-ICP-MS. *J. Anal. At. Spectrom.* **22**, 905–910.

Watson E. B. (2004) A conceptual model for near-surface kinetic controls on the trace- element and stable isotope composition of abiogenic calcite crystals. *Geochim. Cosmochim. Acta* **68**, 1473–1488.

Van Der Weijden C. H. and Van Der Weijden R. D. (2014) Calcite growth: Rate dependence on saturation, on ratios of dissolved calcium and (bi)carbonate and on their complexes. *J. Cryst. Growth* **394**, 137–144.

Welch S. A., Beard B. L., Johnson C. M. and Braterman P. S. (2003) Kinetic and equilibrium Fe isotope fractionation between aqueous Fe(II) and Fe(III). *Geochim. Cosmochim. Acta* **67**, 4231–4250.

Wiederhold J. G., Kraemer S. M., Teutsch N., Borer P. M., Halliday A. N. and Kretzschmar R. (2006) Iron isotope fractionation during proton-promoted, ligand-controlled, and reductive dissolution of goethite. *Environ. Sci. Technol.* **40**, 3787–3793.

Wiesli R. A., Beard B. L. and Johnson C. M. (2004) Experimental determination of Fe isotope fractionation between aqueous Fe (II), siderite and "green rust" in abiotic systems. *Chem. Geol.* **211**, 343–362.

Wilkin R. T. and Barnes H. L. (1997) Formation processes of framboidal pyrite. *Geochim. Cosmochim. Acta* **61**, 323–339.

Wilkin R. T. and Barnes H. L. (1996) Pyrite formation by reactions of iron monosulfides with dissolved inorganic and organic sulfur species. *Geochim. Cosmochim. Acta* **60**, 4167–4179.

Williamson M. A. and Rimstidt J. D. (1994) The kinetics and electrochemical rate-determining step of aqueous pyrite oxidation. *Geochim. Cosmochim. Acta* **58**, 5443–5454.

Wolfe A. L., Stewart B. W., Capo R. C., Liu R., Dzombak D. A., Gordon G. W. and Anbar A. D. (2016) Iron isotope investigation of hydrothermal and sedimentary pyrite and their aqueous dissolution products. *Chem. Geol.* **427**, 73–82.

Wu L., Beard B. L., Roden E. E. and Johnson C. M. (2009) Influence of pH and dissolved Si on Fe isotope fractionation during dissimilatory microbial reduction of hematite. *Geochim. Cosmochim. Acta* **73**, 5584–5599.

Wu L., Druschel G., Findlay A., Beard B. L. and Johnson C. M. (2012) Experimental determination of iron isotope fractionations among Fe^{2+}_{aq}–FeS_{aq}–Mackinawite at low temperatures:

Implications for the rock record. *Geochim. Cosmochim. Acta* **89**, 46–61.

Yamaguchi K. E., Johnson C. M., Beard B. L. and Ohmoto H. (2005) Biogeochemical cycling of iron in the Archean-Paleoproterozoic Earth: constraints from iron isotope variations in sedimentary rocks from the Kaapvaal and Pilbara Cratons. *Chem. Geol.* **218**, 135–169.

Yan R., Kappler A., Muehe E. M. and Knorr K. (2018) Effect of reduced sulfur species on chemolithoautotrophic pyrite oxidation with nitrate. *Geomicrobiol. J.*, 1–10.

Yesavage T., Fantle M. S., Vervoort J., Mathur R., Jin L., Liermann L. J. and Brantley S. L. (2012) Fe cycling in the Shale Hills Critical Zone Observatory, Pennsylvania: an analysis of biogeochemical weathering and Fe isotope fractionation. *Geochim. Cosmochim. Acta* **99**, 18–38.

Yesavage T., Stinchcomb G. E., Fantle M. S., Sak P. B., Kasznel A. and Brantley S. L. (2016) Investigation of a diabase-derived regolith profile from Pennsylvania: mineralogy, chemistry and Fe isotope fractionation. *Geoderma* **273**, 83–97.

Yoshiya K., Nishizawa M., Sawaki Y., Ueno Y., Komiya T., Yamada K., Yoshida N., Hirata T., Wada H. and Maruyama S. (2012) *In situ* iron isotope analyses of pyrite and organic carbon isotope ratios in the Fortescue Group: metabolic variations of a Late Archean ecosystem. *Precambrian Res.* **212–213**, 169–193.

Yoshiya K., Sawaki Y., Hirata T., Maruyama S. and Komiya T. (2015) *In-situ* iron isotope analysis of pyrites in ~3.7 Ga sedimentary protoliths from the Isua supracrustal belt, southern West Greenland. *Chem. Geol.* **401**, 126–139.

Associate editor: Jeffrey C. Alt